# Do Non-dipolar Magnetic Fields Contribute to Spin-down Torques?

Victor See[1] , Sean P. Matt[1] , Adam J. Finley[1] , Colin P. Folsom[2,3], Sudeshna Boro Saikia[4], Jean-Francois Donati[2,3],
Rim Fares[5], Élodie M. Hébrard[11], Moira M. Jardine[6] , Sandra V. Jeffers[7], Stephen C. Marsden[8], Matthew W. Mengel[8],
Julien Morin[9] , Pascal Petit[2,3], Aline A. Vidotto[10] , and Ian A. Waite[8]
and the BCool Collaboration

[1] University of Exeter, Department of Physics & Astronomy, Stocker Road, Devon, Exeter, EX4 4QL, UK; w.see@exeter.ac.uk
[2] Université de Toulouse, UPS-OMP, IRAP, Toulouse, France
[3] CNRS, Institut de Recherche en Astrophysique et Planetologie, 14, avenue Edouard Belin, F-31400 Toulouse, France
[4] University of Vienna, Department of Astrophysics, Tu̇rkenschanzstrasse 17, 1180 Vienna, Austria
[5] Physics Department, United Arab Emirates University, P.O. Box 15551, Al-Ain, United Arab Emirates
[6] SUPA, School of Physics and Astronomy, University of St Andrews, North Haugh, St Andrews KY16 9SS, UK
[7] Universität Göttingen, Institut für Astrophysik, Friedrich-Hund-Platz 1, D-37077 Göttingen, Germany
[8] University of Southern Queensland, Centre for Astrophysics, Toowoomba, QLD 4350, Australia
[9] Laboratoire Univers et Particules de Montpellier, Université de Montpellier, CNRS, F-34095, France
[10] School of Physics, Trinity College Dublin, University of Dublin, Dublin-2, Ireland

## Abstract

Main-sequence low-mass stars are known to spin down as a consequence of their magnetized stellar winds. However, estimating the precise rate of this spin-down is an open problem. The mass-loss rate, angular momentum loss rate, and magnetic field properties of low-mass stars are fundamentally linked, making this a challenging task. Of particular interest is the stellar magnetic field geometry. In this work, we consider whether non-dipolar field modes contribute significantly to the spin-down of low-mass stars. We do this using a sample of stars that have all been previously mapped with Zeeman–Doppler imaging. For a given star, as long as its mass-loss rate is below some critical mass-loss rate, only the dipolar fields contribute to its spin-down torque. However, if it has a larger mass-loss rate, higher-order modes need to be considered. For each star, we calculate this critical mass-loss rate, which is a simple function of the field geometry. Additionally, we use two methods of estimating mass-loss rates for our sample of stars. In the majority of cases, we find that the estimated mass-loss rates do not exceed the critical mass-loss rate; hence, the dipolar magnetic field alone is sufficient to determine the spin-down torque. However, we find some evidence that, at large Rossby numbers, non-dipolar modes may start to contribute.

*Key words:* magnetohydrodynamics (MHD) – stars: evolution – stars: low-mass – stars: magnetic field – stars: rotation – stars: winds, outflows

## 1. Introduction

It is well known that thermally driven stellar winds cause low-mass stars to spin down over their main-sequence lifetimes (e.g., Weber & Davis 1967). Many authors have attempted to model the rotation period evolution of these stars (Gallet & Bouvier 2013, 2015; Brown 2014; Johnstone et al. 2015; Matt et al. 2015; Amard et al. 2016; Blackman & Owen 2016; van Saders et al. 2016; Gondoin 2017; Sadeghi Ardestani et al. 2017; Garraffo et al. 2018; See et al. 2018), but accurately determining angular momentum loss rates is a difficult task. An open question in this context is the impact of magnetic field geometry. Parameter studies using MHD simulations have shown that, when considering only single spherical harmonic modes, the angular momentum loss rate is highest when the field is dipolar and drops dramatically for higher-order field configurations, e.g., quadrupolar, octopolar, etc. (Garraffo et al. 2015; Réville et al. 2015). However, the magnetic fields of real stars are known to be a mixture of many spherical harmonic modes (e.g., DeRosa et al. 2012). It turns out that, when constructing so-called "braking laws" that specify the rate at which stars lose angular momentum, the relevant magnetic parameter to consider is the open flux (Vidotto et al. 2014; Réville et al. 2015; Finley & Matt 2017; Pantolmos & Matt 2017;

Finley & Matt (2018, hereafter F18). This is the flux associated with field lines that extend into interplanetary space, i.e., the field lines along which stellar winds carry away mass and angular momentum.

Previous studies have suggested that the open flux, and hence angular momentum loss rates, is dominated by the dipolar component of the stellar magnetic field (Jardine et al. 2017; See et al. 2017, 2018). However, the open flux is not a directly observable quantity, and attempts to estimate it are difficult and model-dependent. Indeed, there have been some suggestions that higher-order magnetic field modes may play a significant role in the spin-down of low-mass stars (Brown 2014; Garraffo et al. 2018). Recently, Finley & Matt (2017, F18) formulated a braking law in terms of the photospheric field strengths of the dipole, quadrupole, and octopole components of the field. Formulating braking laws in this manner is advantageous because the field geometry can be accounted for without resorting to model-dependent open flux estimates. This braking law can therefore be used to more precisely test the claim that dipole magnetic fields dominate over higher-order geometries when estimating angular momentum loss rates.

To use the braking law of F18), we have to determine the field strengths associated with the dipole, quadrupole, and octopole components of stellar magnetic fields. This is something that the Zeeman–Doppler imaging (ZDI) technique

---
[11] Private astronomer.

can uniquely do. It is a tomographic technique that can reconstruct the large-scale photospheric magnetic field geometries of low-mass stars (Semel 1989; Brown et al. 1991; Donati & Brown 1997; Donati et al. 2006). The magnetic field maps produced from ZDI are expressed in terms of a spherical harmonic decomposition (e.g., see Appendix B of Folsom et al. 2018a), allowing us to take advantage of the F18 braking law.

As well as the magnetic properties of the star, knowledge of the mass-loss rate is also important to accurately determine angular momentum loss rates. Mass-loss rates for low-mass stars are notoriously difficult to determine due to the diffuse nature of their winds. Currently, only indirect methods of measuring stellar mass-loss rates are possible (Wood et al. 2014; Vidotto & Bourrier 2017; Jardine & Collier Cameron 2019). Consequently, when using braking laws, the mass-loss rate is likely to be the least well-constrained input parameter.

In this paper, we investigate whether the dipole magnetic field dominates when calculating angular momentum losses using the F18 braking law. In Section 2, we present this braking law and demonstrate that only the dipole component of the magnetic field contributes to a star's spin-down torque if the star's mass-loss rate is below some critical mass-loss rate. In Section 3, we discuss the magnetic properties of the ZDI sample used in this work. Two methods for estimating mass-loss rates are introduced in Section 4. In Section 5, we calculate the critical mass-loss rates for our sample and analyze which stars are the most likely to have mass-loss rates that exceed the critical mass-loss rate. A discussion of the uncertainties of our work is presented in Section 6. Finally, a discussion and the conclusions of our results are presented in Section 7.

## 2. Finley & Matt (2018) Law

The braking law of F18 takes the form of a twice-broken power law and is given by

$$T = \dot{M}\Omega_\star \langle R_A \rangle^2, \tag{1}$$

where $T$ is the angular momentum loss rate or spin-down torque, $\dot{M}$ is the mass-loss rate, $\Omega_\star = 2\pi/P_{rot}$ is the angular frequency, $P_{rot}$ is the rotation period, and $\langle R_A \rangle$ is the torque-averaged Alfvén radius. Physically, $\langle R_A \rangle$ corresponds to the lever arm of the spin-down torque and is given by

$$\langle R_A \rangle / r_\star = \max \begin{cases} K_d[\mathcal{R}_d^2 \Upsilon]^{m_d}, & \text{(2a)} \\ K_q[(\mathcal{R}_d + \mathcal{R}_q)^2 \Upsilon]^{m_q}, & \text{(2b)} \\ K_o[(\mathcal{R}_d + \mathcal{R}_q + \mathcal{R}_o)^2 \Upsilon]^{m_o}. & \text{(2c)} \end{cases}$$

Here $r_\star$ is the stellar radius, $\Upsilon = \frac{B_\star^2 r_\star^2}{\dot{M} v_{esc}}$ is the wind magnetization, and $v_{esc}$ is the escape velocity of the star. Also, $\mathcal{R}_d = B_d/B_\star$, $\mathcal{R}_q = B_q/B_\star$, and $\mathcal{R}_o = B_o/B_\star$ are the magnetic field ratios where $B_\star = B_d + B_q + B_o$. By definition, $\mathcal{R}_d + \mathcal{R}_q + \mathcal{R}_o = 1$. The subscripts d, q, and o indicate dipole, quadrupole, and octopole, respectively. The precise meaning of $B_d$, $B_q$, and $B_o$ will be further discussed in Section 3. Finally, $K_d = 1.53$, $K_q = 1.7$, $K_o = 1.8$, $m_d = 0.229$, $m_q = 0.134$, and $m_o = 0.087$ are fit parameters obtained from the MHD simulations of F18.

Mathematically, Equation (2) can predict arbitrarily small Alfvén radii if $\Upsilon$ is very small. However, we impose a lower limit on the Alfvén radius of $\sqrt{2/3}\, r_\star$. This is the lever arm associated with a completely unmagnetized and inviscid wind, and smaller
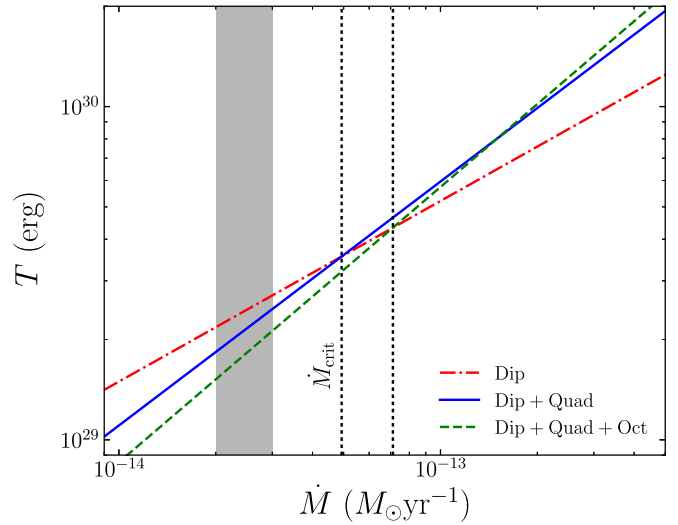


**Figure 1.** Angular momentum loss rate as a function of mass-loss rate using Equations (1) and (2) for solar parameters (see Table 1). The three power laws show the three components of Equation (2): red dotted–dashed line for the dipole component (Equation 2(a)), blue solid line for the dipole + quadrupole component (Equation 2(b)), and green dashed line for the dipole + quadrupole + octopole component (Equation 2(c)). The true angular momentum loss rate is the upper envelope of these three power laws. Black dotted lines indicate the mass-loss rate at which Equations (2(a)) and (b) intersect (labeled as $\dot{M}_{crit}$) and where Equations (2(a)) and (c) intersect. The shaded region roughly indicates the observed solar mass-loss rate.

**Table 1**
Adopted Solar Parameters

|  | Symbol | Adopted Value |
| --- | --- | --- |
| Mass | $M_\odot$ | $1.99 \times 10^{33}$ g |
| Radius | $r_\odot$ | $6.96 \times 10^{10}$ cm |
| Angular frequency | $\Omega_\odot$ | $2.6 \times 10^{-6}$ Hz |
| Dipole field strength | $B_{d,\odot}$ | $0.9^{+0.7}_{-0.6}$ G |
| Quadrupole field strength | $B_{q,\odot}$ | $0.8^{+1.8}_{-0.6}$ G |
| Octopole field strength | $B_{o,\odot}$ | $1.2^{+1.2}_{-0.8}$ G |

**Note.** Note that the upper and lower bounds on the field strengths are the range of values observed in cycle 24 rather than formal errors.

values are unphysical. The factor of $\sqrt{2/3}$ is a consequence of our definition of the angular momentum loss rate in Equation (1). It is a geometric factor that arises when integrating the angular momentum loss rate over all latitudes (e.g., compare with Weber & Davis 1967). We also note that this braking law only accounts for contributions from the dipolar, quadrupolar, and octopolar field modes. Although real stellar magnetic fields contain higher-order spherical harmonic modes, this braking law likely provides a reasonable estimate of the torque. As discussed later in this section, high-order field modes only become relevant at high mass-loss rates. However, if the mass-loss rate of a star is high enough for field modes above the octopolar mode to contribute, the Alfvén radius is likely to be so small that it is close to or below the unmagnetized $r_A = \sqrt{2/3}\, r_\star$ limit.

It is instructive to analyze the behavior of this braking law. As an illustrative example, in Figure 1, we plot angular momentum loss rate as a function of mass-loss rate using Equations (1) and (2) for solar parameters (these are listed in Table 1; the values used for $B_{d,\odot}$, $B_{q,\odot}$, and $B_{o,\odot}$ are discussed in Section 3). While the mass-loss rate of the Sun is relatively

well constrained from observations, the same is not true for other stars. Understanding how this braking law behaves as a function of mass-loss rate is therefore a useful exercise. The three components of Equation (2) are plotted as three separate power laws. The predicted angular momentum loss rate from the F18 braking law is the upper envelope of these three functions.

Figure 1 shows that Equation (2(a)) (red dotted–dashed line) dominates at low mass-loss rates, Equation (2(b)) (blue solid line) dominates at intermediate mass-loss rates, and Equation (2(c)) (green dashed line) dominates at high mass-loss rates. Since Equation (2(a)) depends only on $B_d$, Equation (2(b)) depends on $B_d$ and $B_q$, and Equation (2(c)) depends on $B_d$, $B_q$, and $B_o$, the general trend is that more high-order, non-dipolar field modes are required to properly calculate the spin-down torque at higher mass-loss rates. Physically, this is because high-order field modes decay more rapidly as a function of distance from the star (e.g., see Réville et al. 2015). If the mass-loss rate is low, the Alfvén radius (the lever arm of the spin-down torque) will be large and extend out to a distance where non-dipolar field components have decayed away. However, if the mass-loss rate is large, the Alfvén radius may be small enough that high-order field components have not completely decayed away and must be accounted for.

We can define a critical mass-loss rate, $\dot{M}_{crit}$, below which only the dipole field strength is required to properly determine the angular momentum loss rate of the star. This critical mass-loss rate is given by equating Equations (2(a)) and (b) and solving for the mass-loss rate.[12] It is given by

$$\dot{M}_{crit} = 0.33 \frac{B_\star^2 r_\star^2}{v_{esc}} \frac{\mathcal{R}_d^{4.82}}{(\mathcal{R}_d + \mathcal{R}_q)^{2.82}}, \qquad (3)$$

where we have substituted in the values for $K_d$, $K_q$, $m_d$, and $m_q$. For solar parameters, $\dot{M}_{crit} \sim 5 \times 10^{-14} M_\odot$ yr$^{-1}$. The observed mass-loss rate for the Sun, $\dot{M} \sim 2 \times 10^{-14} M_\odot$ yr$^{-1}$, is lower than this critical mass-loss rate, and, consequently, we only need the dipole component of the solar magnetic field to calculate the solar angular momentum loss rate using the F18 braking law. However, there are caveats to this statement related to the variability of the Sun's magnetic activity that we shall return to in Section 6.3.

## 3. The Stellar Sample and Its Magnetic Properties

The sample of stars we will use in this study is the one presented by See et al. (2019). This sample consists of 85 stars that have had their magnetic fields mapped with ZDI. Some of these stars have been mapped at multiple epochs resulting in 151 magnetic maps. This collection of ZDI maps is drawn from many sources and represents nearly two decades of observations. The parameters (mass, radius, luminosity, and rotation period) used for this work are listed in Table 1 of See et al. (2019) and were generally taken from the original paper that the ZDI map was published in. Additionally, convective

turnover times, $\tau_{cz}$, were calculated using the formulation presented by Cranmer & Saar (2011).[13]

In addition to the parameters listed in Table 1 of See et al. (2019), we also require field strength values for the dipole, quadrupole, and octopole components of the magnetic field for this work, i.e., $B_d$, $B_q$, and $B_o$ in Equation (2). In the MHD simulations of F18, $B_d$, $B_q$, and $B_o$ correspond to field strengths at the rotation pole (or, equivalently in their simulations, the magnetic pole). However, these authors only considered axisymmetric field topologies, whereas ZDI maps contain both axisymmetric and nonaxisymmetric modes. Rather than using polar field values, we will instead use the stellar surface averaged unsigned field strength for each spherical harmonic mode.[14] We shall denote these as $\langle B_{ZDI,d} \rangle$, $\langle B_{ZDI,q} \rangle$, and $\langle B_{ZDI,o} \rangle$. Values for $\langle B_{ZDI,d} \rangle$, $\langle B_{ZDI,q} \rangle$, and $\langle B_{ZDI,o} \rangle$ are shown in Table 2 for our entire sample, along with citations to the original paper each ZDI map is published in.

Numerous studies have shown that magnetic activity indicators scale with the ratio of the rotation period over the convective turnover time, which is known as the Rossby number, Ro $= P_{rot}/\tau_{cz}$. In the top row of Figure 2, we plot $\langle B_{ZDI,d} \rangle$, $\langle B_{ZDI,q} \rangle$, and $\langle B_{ZDI,o} \rangle$ against Ro. Each component follows a relatively tight power-law relation at large Rossby numbers and appears to saturate at small Rossby numbers. This separation into saturated and unsaturated regimes is well known from X-ray studies (Pizzolato et al. 2003; Wright et al. 2011, 2018; Stelzer et al. 2016; Wright & Drake 2016). We have also plotted solar values in each of these panels. These values are calculated using the solar magnetograms from Vidotto et al. (2018) that cover most of cycle 24. For each magnetogram, we calculate a surface averaged poloidal dipole, quadrupole, and octopole field strength. These are then averaged to determine the average poloidal dipole, quadrupole, and octopole field strength over cycle 24 and plotted with magenta squares. The range of possible values over cycle 24 for each of these quantities is plotted with a magenta bar.

For each field component, we perform a three-parameter fit of the form

$$\langle B_{ZDI,i} \rangle = B_{sat,i} \quad \text{for Ro} < \text{Ro}_{crit,i}$$

$$\langle B_{ZDI,i} \rangle = B_{sat,i} \left( \frac{\text{Ro}}{\text{Ro}_{crit,i}} \right)^{\beta_i} \quad \text{for Ro} \geqslant \text{Ro}_{crit,i}, \qquad (4)$$

where the subscript i $= \{d, q, o\}$ represents each of the three components, $B_{sat,i}$ is the field strength in the saturated regime, $\text{Ro}_{crit,i}$ is the critical Rossby number separating the saturated and unsaturated regimes, and $\beta_i$ is the power-law index in the unsaturated regime. As discussed in See et al. (2019), we have excluded the stars with Ro $\lesssim 0.012$ from these fits, since they appear to display bimodal magnetic fields (Donati et al. 2008; Morin et al. 2008b, 2010) for which there is currently no

---

[12] In principle, to properly calculate $\dot{M}_{crit}$, one should calculate the mass-loss rate at which Equation (2(a)) equals Equation (2(b)) and also the mass-loss rate at which Equation (2(a)) equals Equation (2(c)). Then $\dot{M}_{crit}$ is given by the smaller of these two mass-loss rates. However, for the sample of stars presented in Section 3, it turns out that the mass-loss rate at which Equation (2(a)) equals Equation (2(b)) is always smaller than the mass-loss rate at which Equation (2(a)) equals Equation (2(c)).

[13] As noted in See et al. (2019), Cranmer & Saar (2011) stated that this method of calculating convective turnover times is valid for stars with effective temperatures in the range 3300 K $\lesssim T_{eff} \lesssim$ 7000 K. Although a number of our stars have $T_{eff} <$ 3300 K, they all lie in the saturated regime where the magnetic properties of stars, such as field strength, do not change significantly as a function of Rossby number. Therefore, this method of calculating convective turnover times will not greatly affect our results.

[14] More formally, for each harmonic mode, we consider the power in the poloidal component of the component we are interested in. For example, using the formalism shown in Appendix B of Folsom et al. (2018a), $\langle B_{ZDI,q} \rangle$ would be calculated using the $\alpha_{\ell,m}$ and $\beta_{\ell,m}$ coefficients with $\ell = 2$ and $m = \{0, 1, 2\}$ and all other coefficients set to zero.
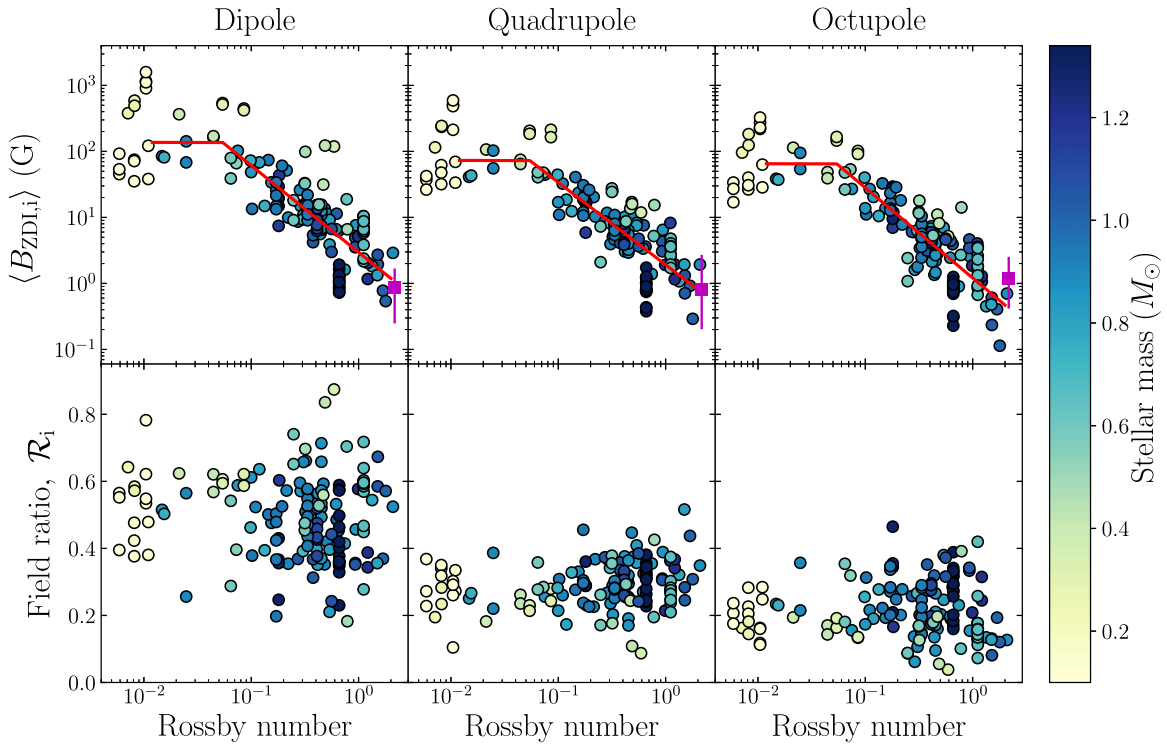
**Figure 2.** Average ZDI magnetic field strength (top row) and field ratio (bottom row) against Rossby number for the magnetic dipole (left), quadrupole (middle), and octopole (right) components. The subscript i = {d, q, o} represents each of the three components. Each point is color-coded by stellar mass. The range of solar values for each component is shown using a magenta bar. A three-parameter fit (Equation (4)) is performed for each component in the top row (solid red line). The best-fit values can be found in Table 3.

definitive explanation. The best-fit values can be found in Table 3, and the corresponding best-fit curves are plotted in red in Figure 2. All three fits have similar $Ro_{crit}$ and $\beta$ values within the error bars. The most notable difference in the fits is that the dipole component has a larger saturation field strength compared to the other two components. The saturation field strength is likely to be the least well-constrained parameter, however, since there are far fewer stars here compared to the unsaturated regime. Additionally, due to observational biases, the Rossby number is correlated to stellar mass in our sample of stars. Although we have parameterized our fit in terms of Rossby number, there may be an additional dependence on stellar mass that is hard to disentangle from the dependence on Rossby number.

As well as the raw field strengths, we can also consider the field ratios defined in Section 2 for our sample of stars, i.e., $\mathcal{R}_i = \langle B_{ZDI,i} \rangle / \sum_j \langle B_{ZDI,j} \rangle$. These are plotted against Rossby number in the bottom row of Figure 2. Each component shows a large amount of scatter with no obvious structure present. On average, $\mathcal{R}_d$ has a higher value than $\mathcal{R}_q$ or $\mathcal{R}_o$, although this is not necessarily true for any individual star.

## 4. Estimating Mass-loss Rates

In this section, we estimate mass-loss rates for our sample of stars. Since estimating mass-loss rates for low-mass stars is difficult and model-dependent, we explore two different methods. Although the main purpose of this section is to estimate mass-loss rates to compare to critical mass-loss rates in Section 5, we will also present the torques and spin-down

timescales associated with these methods, since these are simple to calculate once mass-loss rates have been estimated.

### 4.1. Cranmer & Saar (2011) Method

Our first method of estimating mass-loss rates uses the one-dimensional model of Cranmer & Saar (2011, hereafter CS11), which takes the stellar mass, radius, luminosity, rotation period, and metallicity as inputs. We have chosen to use solar metallicity for all of our stars for simplicity. This model estimates the energy generated from turbulent convective motions in the stellar interior. It then tracks this energy as it travels upward through the photosphere in the form of MHD waves. Eventually, the energy is deposited along open field lines, heating up the local plasma and driving a hot coronal wind.

Figure 3(a) shows the mass-loss rates of our sample estimated with the CS11 model. We have also plotted curves where each line corresponds to mass-loss rates for a fixed stellar mass over a range of Rossby numbers (similar curves are plotted on the other panels of Figure 3). These lines are included to illustrate the behavior of the CS11 model over a range of fixed masses and are intended to aid the reader in interpreting the data points. Additionally, they allow for a rough estimate of mass-loss rates in regions of parameter space that our ZDI sample does not cover. For each line, stellar radii and luminosities, which are required by the CS11 model, are estimated by interpolating over the grid of stellar evolution models of Baraffe et al. (2015) at an age of 2 Gyr. This age is chosen to be older than the zero-age main sequence but younger than the main-sequence turnoff for the types of stars in our sample. We have therefore assumed that the stellar radius

**Table 2**
Numerical Values Used and Derived in This Study for Our Sample of Stars

| Star ID | $\langle B_d \rangle$ (G) | $\langle B_q \rangle$ (G) | $\langle B_o \rangle$ (G) | $\dot{M}$ (CS11) ($M_\odot$ yr$^{-1}$) | $\dot{M}$ (M15) ($M_\odot$ yr$^{-1}$) | $\dot{M}$ (mod M15) ($M_\odot$ yr$^{-1}$) | $\dot{M}_{crit}$ ($M_\odot$ yr$^{-1}$) | $T$ (CS11) (erg) | $T$ (M15) (erg) | $\tau$ (CS11) (Gyr) | $\tau$ (M15) (Gyr) | Reference |
|---|---|---|---|---|---|---|---|---|---|---|---|---|
| *Solar-like Stars* | | | | | | | | | | | | |
| HD 3651 | 2.9 | 1.93 | 0.701 | 4.72E−15 | 1.08E−12 | 3.32E−15 | 6.34E−13 | 1.32E+29 | 2.78E+30 | 224 | 10.7 | P. Petit et al. (2019, in preparation) |
| HD 9986 | 0.539 | 0.291 | 0.114 | 5.63E−14 | 4.87E−12 | 9.03E−14 | 3.85E−14 | 3.60E+29 | 1.29E+31 | 201 | 5.6 | P. Petit et al. (2019, in preparation) |
| HD 10476 | 1.62 | 1.39 | 0.901 | 4.02E−14 | 1.59E−11 | 2.79E−13 | 1.26E−13 | 5.47E+29 | 4.61E+31 | 130 | 1.54 | P. Petit et al. (2019, in preparation) |
| $\kappa$ Cet | 11.4 | 7.61 | 4.44 | 3.36E−13 | 1.28E−11 | 3.49E−14 | 1.08E−11 | 2.67E+31 | 1.99E+32 | 6.81 | 0.915 | do Nascimento et al. (2016) |
| $\epsilon$ Eri (2007) | 11 | 2.93 | 1.47 | 5.05E−14 | 2.86E−11 | 9.93E−14 | 1.28E−11 | 3.97E+30 | 1.45E+32 | 30.3 | 0.827 | Jeffers et al. (2014) |
| $\epsilon$ Eri (2008) | 7.48 | 4.85 | 2.82 | 5.05E−14 | 2.87E−11 | 1.90E−13 | 2.84E−12 | 2.80E+30 | 1.45E+32 | 43 | 0.827 | Jeffers et al. (2014) |
| $\epsilon$ Eri (2010) | 6.47 | 6.36 | 4.65 | 5.05E−14 | 2.71E−11 | 2.42E−13 | 1.26E−12 | 2.45E+30 | 1.45E+32 | 49.1 | 0.827 | Jeffers et al. (2014) |
| $\epsilon$ Eri (2011) | 6.79 | 3.24 | 2.68 | 5.05E−14 | 3.09E−11 | 2.23E−13 | 3.20E−12 | 2.56E+30 | 1.45E+32 | 46.9 | 0.827 | Jeffers et al. (2014) |
| $\epsilon$ Eri (2012) | 12.5 | 5.5 | 3.85 | 5.05E−14 | 2.40E−11 | 7.94E−14 | 1.17E−11 | 4.49E+30 | 1.45E+32 | 26.8 | 0.827 | Jeffers et al. (2014) |
| $\epsilon$ Eri (2013) | 15.6 | 4.03 | 4.06 | 5.05E−14 | 2.14E−11 | 5.48E−14 | 2.64E−11 | 5.48E+30 | 1.45E+32 | 21.9 | 0.827 | Jeffers et al. (2014) |
| HD 39587 | 5.37 | 5.76 | 6.05 | 1.93E−12 | 6.32E−11 | 7.93E−13 | 1.69E−12 | 9.41E+31 | 1.43E+33 | 3.72 | 0.244 | P. Petit et al. (2019, in preparation) |
| HD 56124 | 1.94 | 0.708 | 0.235 | 9.12E−14 | 4.50E−12 | 2.63E−14 | 6.52E−13 | 1.64E+30 | 2.12E+31 | 57.4 | 4.44 | P. Petit et al. (2019, in preparation) |
| HD 72905 | 6.69 | 5.57 | 5.74 | 1.60E−12 | 4.06E−11 | 3.03E−13 | 3.33E−12 | 8.45E+31 | 8.69E+32 | 3.8 | 0.369 | P. Petit et al. (2019, in preparation) |
| HD 73350 | 4.94 | 4.3 | 4.63 | 2.13E−13 | 7.36E−12 | 3.29E−14 | 1.60E−12 | 8.11E+30 | 7.48E+31 | 17.3 | 1.87 | Petit et al. (2008) |
| HD 75332 | 5.14 | 1.91 | 1.86 | 1.31E−12 | 1.01E−11 | 2.96E−14 | 6.91E−12 | 1.16E+32 | 3.79E+32 | 4 | 1.23 | P. Petit et al. (2019, in preparation) |
| HD 76151 | 2.71 | 1.32 | 0.608 | 6.42E−14 | 3.74E−12 | 1.57E−14 | 9.63E−13 | 1.56E+30 | 1.84E+31 | 55.3 | 4.68 | Petit et al. (2008) |
| HD 78366 | 10.4 | 8.25 | 4.03 | 2.97E−13 | 2.14E−12 | 5.49E−15 | 9.40E−12 | 2.61E+31 | 7.61E+31 | 6.69 | 2.29 | P. Petit et al. (2019, in preparation) |
| HD 101501 | 7.61 | 6.48 | 2.57 | 6.09E−14 | 4.25E−12 | 1.17E−14 | 3.48E−12 | 3.42E+30 | 3.55E+31 | 20.2 | 1.94 | P. Petit et al. (2019, in preparation) |
| $\xi$ Boo A (2007) | 21.9 | 10.1 | 7.99 | 2.76E−13 | 3.95E−11 | 1.01E−13 | 4.53E−11 | 4.42E+31 | 6.52E+32 | 5.02 | 0.341 | Morgenthaler et al. (2012) |
| $\xi$ Boo A (2008) | 12.1 | 7.86 | 7.88 | 2.76E−13 | 5.33E−11 | 2.75E−13 | 9.87E−12 | 2.58E+31 | 6.52E+32 | 8.63 | 0.341 | Morgenthaler et al. (2012) |
| $\xi$ Boo A (2009) | 14.6 | 10.9 | 10.4 | 2.76E−13 | 4.79E−11 | 2.00E−13 | 1.23E−11 | 3.06E+31 | 6.52E+32 | 7.26 | 0.341 | Morgenthaler et al. (2012) |
| $\xi$ Boo A (2010 Jan) | 9.04 | 5.43 | 4.73 | 2.76E−13 | 6.23E−11 | 4.51E−13 | 5.96E−12 | 1.97E+31 | 6.52E+32 | 11.3 | 0.341 | Morgenthaler et al. (2012) |
| $\xi$ Boo A (2010 Jun) | 15.2 | 8.01 | 5.64 | 2.76E−13 | 5.17E−11 | 1.87E−13 | 1.93E−11 | 3.17E+31 | 6.52E+32 | 7.01 | 0.341 | Morgenthaler et al. (2012) |
| $\xi$ Boo A (2010 Jul) | 11.2 | 6.34 | 5.04 | 2.76E−13 | 5.83E−11 | 3.16E−13 | 9.60E−12 | 2.39E+31 | 6.52E+32 | 9.32 | 0.341 | Morgenthaler et al. (2012) |
| $\xi$ Boo A (2011) | 14.4 | 6.97 | 3.59 | 2.76E−13 | 5.48E−11 | 2.04E−13 | 1.89E−11 | 3.02E+31 | 6.52E+32 | 7.35 | 0.341 | Morgenthaler et al. (2012) |
| $\xi$ Boo B | 9.34 | 8.15 | 6.34 | 2.70E−15 | 4.20E−11 | 4.35E−13 | 1.63E−12 | 2.89E+29 | 1.15E+32 | 284 | 0.714 | P. Petit et al. (2019, in preparation) |
| 18 Sco | 0.776 | 0.92 | 0.407 | 6.17E−14 | 3.98E−12 | 6.22E−14 | 2.99E−14 | 5.73E+29 | 1.46E+31 | 126 | 4.92 | Petit et al. (2008) |
| HD 166435 | 8.64 | 8.75 | 6.04 | 2.25E−12 | 1.17E−10 | 1.20E−12 | 4.06E−12 | 1.80E+32 | 3.24E+33 | 2.79 | 0.155 | P. Petit et al. (2019, in preparation) |
| HD 175726 | 4.21 | 4.1 | 3.14 | 2.99E−12 | 7.72E−11 | 1.23E−12 | 1.20E−12 | 1.39E+32 | 1.85E+33 | 3.25 | 0.245 | P. Petit et al. (2019, in preparation) |
| HD 190771 | 6.24 | 3.61 | 3.92 | 4.96E−13 | 1.84E−11 | 8.62E−14 | 4.38E−12 | 2.42E+31 | 2.38E+32 | 8.39 | 0.854 | Petit et al. (2008) |
| 61 Cyg A (2007) | 9.77 | 4.76 | 2.62 | 8.03E−16 | 1.18E−12 | 3.03E−15 | 4.75E−12 | 6.94E+28 | 3.62E+30 | 319 | 6.11 | Boro Saikia et al. (2016) |
| 61 Cyg A (2008) | 2.16 | 1.8 | 0.85 | 8.03E−16 | 3.73E−12 | 3.88E−14 | 1.29E−13 | 1.74E+28 | 3.62E+30 | 1.27E+03 | 6.11 | Boro Saikia et al. (2016) |
| 61 Cyg A (2010) | 2.38 | 2.59 | 3.59 | 8.03E−16 | 2.93E−12 | 3.31E−14 | 1.08E−13 | 1.90E+28 | 3.62E+30 | 1.16E+03 | 6.11 | Boro Saikia et al. (2016) |
| 61 Cyg A (2013) | 8.33 | 3.79 | 1.73 | 8.03E−16 | 1.55E−12 | 3.97E−15 | 3.68E−12 | 6.00E+28 | 3.62E+30 | 369 | 6.11 | Boro Saikia et al. (2016) |
| 61 Cyg A (2014) | 6.91 | 3.33 | 1.56 | 8.03E−16 | 2.12E−12 | 5.44E−15 | 2.40E−12 | 5.05E+28 | 3.62E+30 | 438 | 6.11 | Boro Saikia et al. (2016) |
| 61 Cyg A (2015 Aug) | 10.4 | 4.05 | 1.83 | 8.03E−16 | 1.06E−12 | 2.71E−15 | 6.58E−12 | 7.37E+28 | 3.62E+30 | 300 | 6.11 | Boro Saikia et al. (2016) |
| 61 Cyg A (2015 Oct) | 6.88 | 2.71 | 1.82 | 8.03E−16 | 2.14E−12 | 5.48E−15 | 2.83E−12 | 5.03E+28 | 3.62E+30 | 439 | 6.11 | Boro Saikia et al. (2018) |
| 61 Cyg A (2015 Dec) | 5.84 | 2.66 | 1.32 | 8.03E−16 | 2.51E−12 | 7.22E−15 | 1.81E−12 | 4.34E+28 | 3.62E+30 | 510 | 6.11 | Boro Saikia et al. (2018) |
| 61 Cyg A (2016) | 6.23 | 3.67 | 3.44 | 8.03E−16 | 2.24E−12 | 6.47E−15 | 1.61E−12 | 4.60E+28 | 3.62E+30 | 481 | 6.11 | Boro Saikia et al. (2018) |
| 61 Cyg A (Jul 2017) | 6.62 | 1.93 | 0.672 | 8.03E−16 | 2.28E−12 | 5.84E−15 | 3.25E−12 | 4.86E+28 | 3.62E+30 | 455 | 6.11 | Boro Saikia et al. (2018) |
| 61 Cyg A (2017 Dec) | 3.84 | 1.71 | 0.928 | 8.03E−16 | 3.29E−12 | 1.47E−14 | 7.97E−13 | 2.95E+28 | 3.62E+30 | 749 | 6.11 | Boro Saikia et al. (2018) |
| 61 Cyg A (2018) | 8.74 | 3.61 | 2.32 | 8.03E−16 | 1.43E−12 | 3.66E−15 | 4.40E−12 | 6.27E+28 | 3.62E+30 | 353 | 6.11 | Boro Saikia et al. (2018) |
| HN Peg (2007) | 9.62 | 6.61 | 4.01 | 2.01E−12 | 4.98E−11 | 2.36E−13 | 9.12E−12 | 1.62E+32 | 1.29E+33 | 2.55 | 0.321 | Boro Saikia et al. (2015) |
| HN Peg (2008) | 6.27 | 4.09 | 4.35 | 2.01E−12 | 5.70E−11 | 4.86E−13 | 4.11E−12 | 1.09E+32 | 1.29E+33 | 3.78 | 0.321 | Boro Saikia et al. (2015) |
| HN Peg (2009) | 6.83 | 3.86 | 4.2 | 2.01E−12 | 5.67E−11 | 4.22E−13 | 5.67E−12 | 1.18E+32 | 1.29E+33 | 3.49 | 0.321 | Boro Saikia et al. (2015) |
| HN Peg (2010) | 9.15 | 6.17 | 5.82 | 2.01E−12 | 4.89E−11 | 2.57E−13 | 8.43E−12 | 1.55E+32 | 1.29E+33 | 2.67 | 0.321 | Boro Saikia et al. (2015) |

**Table 2**
(Continued)

| Star ID | $\langle B_{\rm d}\rangle$ (G) | $\langle B_{\rm q}\rangle$ (G) | $\langle B_{\rm o}\rangle$ (G) | $\dot{M}$ (CS11) ($M_\odot$ yr$^{-1}$) | $\dot{M}$ (M15) ($M_\odot$ yr$^{-1}$) | $\dot{M}$ (mod M15) ($M_\odot$ yr$^{-1}$) | $\dot{M}_{\rm crit}$ ($M_\odot$ yr$^{-1}$) | $T$ (CS11) (erg) | $T$ (M15) (erg) | $\tau$ (CS11) (Gyr) | $\tau$ (M15) (Gyr) | Reference |
|---|---|---|---|---|---|---|---|---|---|---|---|---|
| HN Peg (2011) | 7.72 | 6.8 | 5.94 | 2.01E−12 | 4.96E−11 | 3.43E−13 | 4.32E−12 | 1.32E+32 | 1.29E+33 | 3.12 | 0.321 | Boro Saikia et al. (2015) |
| HN Peg (2013) | 13.7 | 8.04 | 4.56 | 2.01E−12 | 4.08E−11 | 1.31E−13 | 2.18E−11 | 2.23E+32 | 1.29E+33 | 1.85 | 0.321 | Boro Saikia et al. (2015) |
| HD 219134 | 1.33 | 1.93 | 0.479 | 1.46E−15 | 2.83E−12 | 3.73E−14 | 3.46E−14 | 2.45E+28 | 3.65E+30 | 1070 | 7.2 | Folsom et al. (2018b) |
| AV 1693 | 13.5 | 17.1 | 7.67 | 1.65E−13 | 1.49E−11 | 5.66E−14 | 4.89E−12 | 1.47E+31 | 2.09E+32 | 10.1 | 0.708 | Folsom et al. (2018a) |
| AV 1826 | 9.5 | 10.2 | 7.37 | 8.85E−14 | 2.89E−11 | 1.67E−13 | 2.94E−12 | 6.67E+30 | 2.39E+32 | 19.5 | 0.544 | Folsom et al. (2018a) |
| AV 2177 | 6.23 | 3.52 | 2.2 | 1.12E−13 | 3.40E−11 | 2.71E−13 | 2.54E−12 | 4.89E+30 | 2.00E+32 | 30.6 | 0.746 | Folsom et al. (2018a) |
| AV 523 | 9.32 | 7.36 | 6.76 | 2.23E−14 | 2.83E−11 | 1.72E−13 | 3.39E−12 | 1.90E+30 | 1.46E+32 | 51.3 | 0.668 | Folsom et al. (2018a) |
| EP Eri | 14.9 | 9.55 | 1.61 | 7.68E−14 | 6.30E−11 | 3.01E−13 | 1.06E−11 | 9.23E+30 | 4.91E+32 | 19.4 | 0.365 | Folsom et al. (2018a) |
| HH Leo | 15.5 | 8.78 | 6.14 | 3.27E−13 | 5.74E−11 | 2.19E−13 | 1.84E−11 | 3.80E+31 | 7.77E+32 | 6.56 | 0.321 | Folsom et al. (2018a) |
| Mel 25-151 | 12 | 7.8 | 4.77 | 5.52E−14 | 2.99E−11 | 1.15E−13 | 9.37E−12 | 6.18E+30 | 2.34E+32 | 18.8 | 0.498 | Folsom et al. (2018a) |
| Mel 25-179 | 15.5 | 7.89 | 5.6 | 8.56E−14 | 2.77E−11 | 7.76E−14 | 2.15E−11 | 1.15E+31 | 2.76E+32 | 10.9 | 0.453 | Folsom et al. (2018a) |
| Mel 25-21 | 10.5 | 4.38 | 2.83 | 1.70E−13 | 2.88E−11 | 9.50E−14 | 1.41E−11 | 1.48E+31 | 2.74E+32 | 9.31 | 0.503 | Folsom et al. (2018a) |
| Mel 25-43 | 5.59 | 3.05 | 1.35 | 7.59E−14 | 3.79E−11 | 3.31E−13 | 2.26E−12 | 3.43E+30 | 1.93E+32 | 35.7 | 0.634 | Folsom et al. (2018a) |
| Mel 25-5 | 6.71 | 3.04 | 2.14 | 8.32E−14 | 4.45E−11 | 2.89E−13 | 5.51E−12 | 6.22E+30 | 3.10E+32 | 18.5 | 0.371 | Folsom et al. (2018a) |
| TYC 1987-509-1 | 11.4 | 10.2 | 5.51 | 1.53E−13 | 1.72E−11 | 6.45E−14 | 5.83E−12 | 1.16E+31 | 1.85E+32 | 12.2 | 0.769 | Folsom et al. (2018a) |
| V447 Lac | 9.95 | 10.3 | 7.8 | 3.06E−13 | 1.38E−10 | 1.71E−12 | 3.39E−12 | 2.95E+31 | 1.90E+33 | 10.3 | 0.159 | Folsom et al. (2016) |
| DX Leo | 26.1 | 11.7 | 6.01 | 3.11E−13 | 5.14E−11 | 1.32E−13 | 6.10E−11 | 5.93E+31 | 9.45E+32 | 4.21 | 0.264 | Folsom et al. (2016) |
| V439 And | 9.51 | 4.61 | 2.46 | 4.35E−13 | 7.31E−11 | 4.29E−13 | 1.01E−11 | 3.59E+31 | 9.04E+32 | 6.59 | 0.262 | Folsom et al. (2016) |
| *Young Suns* | | | | | | | | | | | | |
| AB Dor (2001) | 68.1 | 103 | 94.8 | 7.81E−13 | 2.73E−11 | 6.99E−14 | 1.35E−10 | 4.23E+33 | 2.90E+34 | 0.621 | 0.0905 | Donati et al. (2003) |
| AB Dor (2002) | 142 | 55.4 | 54.1 | 7.81E−13 | 7.87E−12 | 2.02E−14 | 3.11E−09 | 8.30E+33 | 2.90E+34 | 0.317 | 0.0905 | Donati et al. (2003) |
| BD−16351 | 34 | 23.6 | 13.8 | 4.42E−13 | 8.71E−11 | 2.28E−13 | 8.20E−11 | 1.99E+32 | 3.52E+33 | 2.1 | 0.119 | Folsom et al. (2016) |
| HII 296 | 65.4 | 32.5 | 27 | 3.23E−13 | 2.93E−11 | 7.52E−14 | 4.93E−10 | 4.47E+32 | 5.14E+33 | 1.15 | 0.0999 | Folsom et al. (2016) |
| HII 739 | 7.44 | 5.89 | 6.99 | 7.37E−12 | 2.46E−10 | 4.07E−12 | 4.84E−12 | 8.74E+32 | 1.48E+34 | 1.48 | 0.0872 | Folsom et al. (2016) |
| HIP 12545 | 73.9 | 40.8 | 32.7 | 8.07E−14 | 2.53E−11 | 6.49E−14 | 7.89E−10 | 1.96E+32 | 4.41E+33 | 1.56 | 0.0693 | Folsom et al. (2016) |
| HIP 76768 | 68.2 | 18.6 | 20.4 | 5.01E−14 | 2.34E−11 | 6.01E−14 | 7.21E−10 | 9.24E+31 | 2.59E+33 | 3.17 | 0.113 | Folsom et al. (2016) |
| Lo Peg | 81.3 | 43.1 | 37.3 | 4.43E−14 | 1.63E−11 | 4.19E−14 | 3.34E−10 | 4.07E+32 | 1.00E+34 | 5.6 | 0.228 | Folsom et al. (2016) |
| PELS 031 | 13.4 | 11 | 11.1 | 4.99E−13 | 1.67E−10 | 1.16E−12 | 1.60E−11 | 2.01E+32 | 8.03E+33 | 2.94 | 0.0734 | Folsom et al. (2016) |
| PW And | 102 | 44.5 | 27 | 1.79E−13 | 1.30E−11 | 3.33E−14 | 8.97E−10 | 4.21E+32 | 4.29E+33 | 1.63 | 0.16 | Folsom et al. (2016) |
| TYC 0486-4943-1 | 14.9 | 12.4 | 10.5 | 4.15E−14 | 9.83E−11 | 7.33E−13 | 7.55E−12 | 1.08E+31 | 1.29E+33 | 23.9 | 0.198 | Folsom et al. (2016) |
| TYC 5164-567-1 | 51.6 | 20.4 | 18.1 | 3.15E−13 | 4.39E−11 | 1.13E−13 | 3.36E−10 | 1.72E+32 | 2.50E+33 | 1.66 | 0.114 | Folsom et al. (2016) |
| TYC 6349-0200-1 | 48.6 | 17 | 13.8 | 4.64E−14 | 4.47E−11 | 1.15E−13 | 4.06E−10 | 1.02E+32 | 4.22E+33 | 3.49 | 0.0843 | Folsom et al. (2016) |
| TYC 6878-0195-1 | 43.5 | 16.7 | 12 | 3.68E−13 | 8.03E−11 | 2.06E−13 | 6.32E−10 | 4.81E+32 | 8.92E+33 | 0.766 | 0.0414 | Folsom et al. (2016) |
| HD 6569 | 16.7 | 5.12 | 3.43 | 1.12E−13 | 5.23E−11 | 1.65E−13 | 2.93E−11 | 1.41E+31 | 4.42E+32 | 12 | 0.385 | Folsom et al. (2018a) |
| HIP 10272 | 11 | 3.94 | 1.78 | 2.16E−13 | 7.69E−11 | 4.31E−13 | 1.26E−11 | 1.86E+31 | 6.86E+32 | 11.7 | 0.319 | Folsom et al. (2018a) |
| BD−072388 | 84.5 | 41.2 | 38.4 | 2.48E−13 | 1.78E−11 | 4.57E−14 | 5.58E−10 | 2.28E+33 | 2.32E+34 | 1.63 | 0.16 | Folsom et al. (2018a) |
| HD 141943 (2007) | 29.4 | 23.8 | 29.3 | 2.54E−11 | 1.77E−10 | 4.55E−13 | 1.89E−10 | 1.39E+34 | 3.97E+34 | 8.66E−02 | 0.0302 | Marsden et al. (2011) |
| HD 141943 (2009) | 19.5 | 16.4 | 9.5 | 2.54E−11 | 2.40E−10 | 9.09E−13 | 7.96E−11 | 9.52E+33 | 3.97E+34 | 0.126 | 0.0302 | Marsden et al. (2011) |
| HD 141943 (2010) | 14.9 | 17.4 | 28.1 | 2.54E−11 | 2.35E−10 | 1.43E−12 | 2.91E−11 | 7.43E+33 | 3.97E+34 | 0.161 | 0.0302 | Marsden et al. (2011) |
| HD 35296 (2007) | 6.69 | 3.66 | 4.78 | 3.56E−12 | 2.70E−11 | 1.31E−13 | 6.61E−12 | 2.49E+32 | 1.05E+33 | 2.05 | 0.484 | Waite et al. (2015) |
| HD 35296 (2008) | 3 | 4.76 | 4.6 | 3.56E−12 | 2.94E−11 | 4.48E−13 | 3.10E−13 | 1.90E+32 | 1.05E+33 | 2.69 | 0.484 | Waite et al. (2015) |
| HD 29615 | 60.6 | 26.1 | 28.6 | 3.77E−12 | 3.56E−11 | 9.13E−14 | 5.63E−10 | 2.19E+33 | 7.38E+33 | 0.288 | 0.0854 | Waite et al. (2015) |
| EK Dra (2006) | 25.9 | 18.6 | 16.6 | 1.40E−12 | 1.14E−10 | 3.85E−13 | 5.26E−11 | 4.09E+32 | 5.15E+33 | 1.3 | 0.104 | Waite et al. (2017) |
| EK Dra (2007 Jan) | 33.8 | 19.8 | 13.5 | 1.40E−12 | 9.59E−11 | 2.46E−13 | 1.12E−10 | 5.21E+32 | 5.15E+33 | 1.02 | 0.104 | Waite et al. (2017) |
| EK Dra (2007 Feb) | 14.9 | 12 | 13.6 | 1.40E−12 | 1.45E−10 | 9.88E−13 | 1.49E−11 | 2.45E+32 | 5.15E+33 | 2.17 | 0.104 | Waite et al. (2017) |
| EK Dra (2008) | 21.5 | 10.7 | 12.7 | 1.40E−12 | 1.39E−10 | 5.28E−13 | 5.36E−11 | 3.44E+32 | 5.15E+33 | 1.55 | 0.104 | Waite et al. (2017) |
| EK Dra (2012) | 13.3 | 30.7 | 23.4 | 1.40E−12 | 1.15E−10 | 1.19E−12 | 2.19E−12 | 2.22E+32 | 5.15E+33 | 2.4 | 0.104 | Waite et al. (2017) |

See et al.

**Table 2**
(Continued)

| Star ID | $\langle B_{\rm d}\rangle$ (G) | $\langle B_{\rm q}\rangle$ (G) | $\langle B_{\rm o}\rangle$ (G) | $\dot{M}$ (CS11) ($M_\odot$ yr$^{-1}$) | $\dot{M}$ (M15) ($M_\odot$ yr$^{-1}$) | $\dot{M}$ (mod M15) ($M_\odot$ yr$^{-1}$) | $\dot{M}_{\rm crit}$ ($M_\odot$ yr$^{-1}$) | $T$ (CS11) (erg) | $T$ (M15) (erg) | $\tau$ (CS11) (Gyr) | $\tau$ (M15) (Gyr) | Reference |
|---|---|---|---|---|---|---|---|---|---|---|---|---|
| *Hot Jupiter Hosts* | | | | | | | | | | | | |
| τ Boo (2008 Jan) | 0.889 | 0.794 | 0.873 | 7.66E−12 | 5.71E−11 | 1.14E−12 | 1.19E−13 | 4.54E+32 | 2.39E+33 | 2.17 | 0.413 | Fares et al. (2009) |
| τ Boo (Jun 8) | 0.868 | 0.778 | 0.772 | 7.66E−12 | 5.84E−11 | 1.17E−12 | 1.13E−13 | 4.45E+32 | 2.39E+33 | 2.21 | 0.413 | Fares et al. (2009) |
| τ Boo (2008 Jul) | 0.725 | 0.784 | 0.696 | 7.66E−12 | 6.07E−11 | 1.21E−12 | 6.06E−14 | 4.31E+32 | 2.39E+33 | 2.28 | 0.413 | Fares et al. (2009) |
| τ Boo (2009) | 1.23 | 1 | 0.831 | 7.66E−12 | 5.29E−11 | 1.03E−12 | 2.58E−13 | 4.84E+32 | 2.39E+33 | 2.03 | 0.413 | Fares et al. (2013) |
| τ Boo (2010) | 1.35 | 1.19 | 1.04 | 7.66E−12 | 4.95E−11 | 9.36E−13 | 2.80E−13 | 5.11E+32 | 2.39E+33 | 1.93 | 0.413 | Fares et al. (2013) |
| τ Boo (2011 Jan) | 1.63 | 0.745 | 0.899 | 7.66E−12 | 5.14E−11 | 9.86E−13 | 8.37E−13 | 4.95E+32 | 2.39E+33 | 1.99 | 0.413 | Fares et al. (2013) |
| τ Boo (2011 May) | 0.742 | 1.23 | 1.25 | 7.66E−12 | 5.18E−11 | 1.03E−12 | 3.18E−14 | 4.92E+32 | 2.39E+33 | 2 | 0.413 | Mengel et al. (2016) |
| τ Boo (2013 May) | 1.32 | 1.26 | 1.08 | 7.66E−12 | 4.91E−11 | 9.28E−13 | 2.41E−13 | 5.14E+32 | 2.39E+33 | 1.91 | 0.413 | Mengel et al. (2016) |
| τ Boo (2013 Dec) | 1.92 | 1.74 | 0.925 | 7.66E−12 | 4.46E−11 | 7.18E−13 | 5.49E−13 | 5.56E+32 | 2.39E+33 | 1.77 | 0.413 | Mengel et al. (2016) |
| τ Boo (2014) | 1.05 | 0.893 | 0.965 | 7.66E−12 | 5.41E−11 | 1.08E−12 | 1.75E−13 | 4.75E+32 | 2.39E+33 | 2.07 | 0.413 | Mengel et al. (2016) |
| τ Boo (2015 Jan) | 1.14 | 1.02 | 1.06 | 7.66E−12 | 5.18E−11 | 1.03E−12 | 1.96E−13 | 4.92E+32 | 2.39E+33 | 2 | 0.413 | Mengel et al. (2016) |
| τ Boo (2015 Apr 2) | 1.07 | 0.435 | 0.309 | 7.66E−12 | 6.60E−11 | 1.32E−12 | 3.95E−13 | 4.03E+32 | 2.39E+33 | 2.44 | 0.413 | Mengel et al. (2016) |
| τ Boo (2015 Apr 13) | 0.826 | 0.378 | 0.229 | 7.66E−12 | 7.28E−11 | 1.45E−12 | 2.15E−13 | 3.71E+32 | 2.39E+33 | 2.65 | 0.413 | Mengel et al. (2016) |
| τ Boo (2015 Apr 20) | 1 | 0.426 | 0.321 | 7.66E−12 | 6.70E−11 | 1.34E−12 | 3.37E−13 | 3.98E+32 | 2.39E+33 | 2.47 | 0.413 | Mengel et al. (2016) |
| τ Boo (2015 May) | 1.34 | 0.811 | 0.745 | 7.66E−12 | 5.41E−11 | 1.06E−12 | 4.35E−13 | 4.75E+32 | 2.39E+33 | 2.07 | 0.413 | Mengel et al. (2016) |
| HD 73256 | 3.54 | 3.07 | 3.44 | 9.98E−14 | 7.89E−12 | 5.97E−14 | 6.41E−13 | 2.56E+30 | 4.91E+31 | 48.8 | 2.54 | Fares et al. (2013) |
| HD 102195 | 6.62 | 3.37 | 2.45 | 7.87E−14 | 1.59E−11 | 7.30E−14 | 3.67E−12 | 3.67E+30 | 8.94E+31 | 28 | 1.15 | Fares et al. (2013) |
| HD 130322 | 1.82 | 1.08 | 0.451 | 1.72E−14 | 4.01E−12 | 3.27E−14 | 2.60E−13 | 2.47E+29 | 8.90E+30 | 164 | 4.56 | Fares et al. (2013) |
| HD 179949 (2007) | 1.17 | 1.16 | 1.07 | 5.10E−13 | 9.09E−12 | 1.53E−13 | 1.12E−13 | 1.33E+31 | 1.40E+32 | 22.1 | 2.1 | Fares et al. (2012) |
| HD 179949 (2009) | 2.04 | 1.94 | 1.29 | 5.10E−13 | 7.55E−12 | 6.60E−14 | 3.67E−13 | 1.78E+31 | 1.40E+32 | 16.6 | 2.1 | Fares et al. (2012) |
| HD 189733 (2007) | 3.88 | 7.53 | 7 | 3.94E−14 | 1.71E−11 | 2.44E−13 | 1.64E−13 | 1.22E+30 | 8.94E+31 | 74.7 | 1.02 | Fares et al. (2010) |
| HD 189733 (2008) | 9.17 | 8.26 | 5.71 | 3.94E−14 | 1.48E−11 | 6.57E−14 | 3.13E−12 | 2.67E+30 | 8.94E+31 | 34 | 1.02 | Fares et al. (2010) |
| *M Dwarf Stars* | | | | | | | | | | | | |
| CE Boo | 98.7 | 25 | 17.9 | 9.46E−17 | 1.61E−12 | 4.14E−15 | 3.69E−10 | 1.44E+29 | 2.82E+31 | 180 | 0.916 | Donati et al. (2008) |
| DS Leo (2007) | 33.1 | 27.5 | 12.2 | 2.72E−16 | 1.35E−11 | 3.46E−14 | 2.08E−11 | 1.71E+29 | 5.99E+31 | 244 | 0.696 | Donati et al. (2008) |
| DS Leo (2008) | 32.6 | 24.3 | 11.6 | 2.72E−16 | 1.38E−11 | 3.55E−14 | 2.31E−11 | 1.68E+29 | 5.99E+31 | 247 | 0.696 | Donati et al. (2008) |
| GJ 182 | 72.6 | 44.3 | 40.1 | 3.36E−15 | 1.94E−11 | 4.98E−14 | 3.96E−10 | 1.74E+31 | 1.91E+33 | 12.7 | 0.116 | Donati et al. (2008) |
| GJ 49 | 15.7 | 8.71 | 5.32 | 1.82E−16 | 1.25E−11 | 3.91E−14 | 7.11E−12 | 4.93E+28 | 2.29E+31 | 612 | 1.32 | Donati et al. (2008) |
| AD Leo (2007) | 162 | 74.6 | 48.6 | 6.12E−17 | 2.44E−12 | 6.26E−15 | 5.09E−10 | 8.20E+29 | 2.55E+32 | 152 | 0.489 | Morin et al. (2008b) |
| AD Leo (2008) | 170 | 64.5 | 39.3 | 6.12E−17 | 2.25E−12 | 5.78E−15 | 6.57E−10 | 8.56E+29 | 2.55E+32 | 146 | 0.489 | Morin et al. (2008b) |
| DT Vir (2007) | 79.3 | 40.6 | 26.5 | 5.98E−16 | 1.25E−11 | 3.22E−14 | 2.14E−10 | 3.03E+30 | 6.67E+32 | 70.1 | 0.319 | Donati et al. (2008) |
| DT Vir (2008) | 39 | 48.5 | 47.9 | 5.98E−16 | 3.30E−11 | 1.07E−13 | 1.69E−11 | 1.58E+30 | 6.67E+32 | 134 | 0.319 | Donati et al. (2008) |
| EQ Peg A | 366 | 107 | 114 | 4.78E−17 | 5.63E−13 | 1.44E−15 | 3.09E−09 | 2.50E+30 | 4.03E+32 | 87.2 | 0.542 | Morin et al. (2008b) |
| EQ Peg B | 379 | 115 | 96 | 1.73E−18 | 2.99E−11 | 7.68E−16 | 1.74E−09 | 4.37E+29 | 3.01E+32 | 435 | 0.631 | Morin et al. (2008b) |
| EV Lac (2006) | 447 | 213 | 102 | 1.80E−17 | 3.11E−13 | 7.99E−16 | 2.37E−09 | 2.77E+29 | 5.49E+31 | 113 | 0.57 | Morin et al. (2008b) |
| EV Lac (2007) | 420 | 164 | 91.5 | 1.80E−17 | 3.45E−13 | 8.86E−16 | 2.48E−09 | 2.62E+29 | 5.49E+31 | 119 | 0.57 | Morin et al. (2008b) |
| DX Cnc (2007) | 92.3 | 37.2 | 33.8 | 4.54E−21 | 1.02E−12 | 2.61E−15 | 1.70E−11 | 3.87E+26 | 1.30E+31 | 4.13E+04 | 1.23 | Morin et al. (2010) |
| DX Cnc (2008) | 45.3 | 42.2 | 27.1 | 4.54E−21 | 2.82E−12 | 8.68E−15 | 1.67E−12 | 2.02E+26 | 1.30E+31 | 7.93E+04 | 1.23 | Morin et al. (2010) |
| DX Cnc (2009) | 53.5 | 26.4 | 17 | 4.54E−21 | 2.55E−12 | 6.55E−15 | 4.81E−12 | 2.35E+26 | 1.30E+31 | 6.80E+04 | 1.23 | Morin et al. (2010) |
| GJ 1156 (2007) | 35.3 | 31.9 | 26.5 | 2.92E−19 | 5.70E−12 | 2.02E−14 | 2.27E−12 | 4.33E+27 | 4.61E+31 | 8150 | 0.765 | Morin et al. (2010) |
| GJ 1156 (2008) | 74.9 | 62 | 40.1 | 2.92E−19 | 2.21E−12 | 5.66E−15 | 1.15E−11 | 8.63E+27 | 4.61E+31 | 4090 | 0.765 | Morin et al. (2010) |
| GJ 1156 (2009) | 71.4 | 47.7 | 30.7 | 2.92E−19 | 2.39E−12 | 6.14E−15 | 1.35E−11 | 8.26E+27 | 4.61E+31 | 4270 | 0.765 | Morin et al. (2010) |
| GJ 1245 B (2006) | 122 | 69.4 | 63.1 | 1.09E−19 | 7.98E−13 | 2.05E−15 | 3.60E−11 | 3.71E+27 | 1.95E+31 | 4410 | 0.841 | Morin et al. (2010) |
| GJ 1245 B (2008) | 38.2 | 33.6 | 28.5 | 1.09E−19 | 4.39E−12 | 1.45E−14 | 2.14E−12 | 1.28E+27 | 1.95E+31 | 1.28E+04 | 0.841 | Morin et al. (2010) |
| OT Ser | 66.3 | 47.6 | 53.4 | 2.82E−16 | 1.56E−11 | 4.00E−14 | 8.85E−11 | 1.14E+30 | 4.23E+32 | 134 | 0.361 | Donati et al. (2008) |
| V374 Peg (2005) | 588 | 235 | 183 | 4.92E−18 | 1.64E−13 | 4.22E−16 | 4.30E−09 | 1.42E+30 | 4.03E+32 | 157 | 0.556 | Morin et al. (2008a) |

**Table 2**
(Continued)

| Star ID | $\langle B_{\rm d} \rangle$ (G) | $\langle B_{\rm q} \rangle$ (G) | $\langle B_{\rm o} \rangle$ (G) | $\dot{M}$ (CS11) ($M_\odot$ yr$^{-1}$) | $\dot{M}$ (M15) ($M_\odot$ yr$^{-1}$) | $\dot{M}$ (mod M15) ($M_\odot$ yr$^{-1}$) | $\dot{M}_{\rm crit}$ ($M_\odot$ yr$^{-1}$) | $T$ (CS11) (erg) | $T$ (M15) (erg) | $\tau$ (CS11) (Gyr) | $\tau$ (M15) (Gyr) | Reference |
|---|---|---|---|---|---|---|---|---|---|---|---|---|
| V374 Peg (2006) | 491 | 243 | 124 | 4.92E−18 | 2.23E−13 | 5.71E−16 | 2.50E−09 | 1.21E+30 | 4.03E+32 | 186 | 0.556 | Morin et al. (2008a) |
| WX UMa (2006) | 904 | 511 | 275 | 1.28E−20 | 2.14E−14 | 5.48E−17 | 1.49E−09 | 4.25E+27 | 1.00E+31 | 2.22E+03 | 0.94 | Morin et al. (2010) |
| WX UMa (2007) | 1160 | 485 | 219 | 1.28E−20 | 1.41E−14 | 3.61E−17 | 3.22E−09 | 5.33E+27 | 1.00E+31 | 1.77E+03 | 0.94 | Morin et al. (2010) |
| WX UMa (2008) | 1110 | 593 | 326 | 1.28E−20 | 1.50E−14 | 3.85E−17 | 2.41E−09 | 5.15E+27 | 1.00E+31 | 1.83E+03 | 0.94 | Morin et al. (2010) |
| WX UMa (2009) | 1590 | 212 | 229 | 1.28E−20 | 8.23E−15 | 2.11E−17 | 1.15E−08 | 7.13E+27 | 1.00E+31 | 1.32E+03 | 0.94 | Morin et al. (2010) |
| YZ CMi (2007) | 540 | 205 | 146 | 1.47E−17 | 2.27E−13 | 5.81E−16 | 3.86E−09 | 4.18E+29 | 7.80E+31 | 118 | 0.633 | Morin et al. (2008b) |
| YZ CMi (2008) | 514 | 185 | 166 | 1.47E−17 | 2.47E−13 | 6.33E−16 | 3.64E−09 | 4.00E+29 | 7.80E+31 | 123 | 0.633 | Morin et al. (2008b) |
| GJ 176 | 6.6 | 15.4 | 14.2 | 9.04E−18 | 2.13E−12 | 1.46E−14 | 1.30E−13 | 1.66E+27 | 2.31E+30 | 6.12E+03 | 4.4 | É. M. Hébrard et al. (2019, in preparation) |
| GJ 205 | 18.8 | 5.22 | 2.7 | 6.44E−17 | 1.41E−12 | 3.61E−15 | 2.06E−11 | 2.28E+28 | 5.12E+30 | 903 | 4.01 | Hébrard et al. (2016) |
| GJ 358 | 123 | 15.9 | 8.15 | 1.22E−17 | 1.96E−13 | 5.03E−16 | 7.25E−10 | 2.96E+28 | 5.65E+30 | 372 | 1.95 | Hébrard et al. (2016) |
| GJ 479 | 31.4 | 13.7 | 11 | 1.81E−17 | 2.32E−12 | 5.95E−15 | 2.54E−11 | 1.20E+28 | 7.02E+30 | 1.02E+03 | 1.75 | Hébrard et al. (2016) |
| GJ 674 | 119 | 11.9 | 5.21 | 1.16E−18 | 8.00E−14 | 2.05E−16 | 7.55E−10 | 5.60E+27 | 2.35E+30 | 856 | 2.04 | É. M. Hébrard et al. (2019, in preparation) |
| GJ 846 (2013) | 9.09 | 2.1 | 1.08 | 4.96E−16 | 8.01E−11 | 7.81E−13 | 5.21E−12 | 1.06E+29 | 1.45E+32 | 554 | 0.404 | Hébrard et al. (2016) |
| GJ 846 (2014) | 18.2 | 7.29 | 2.42 | 4.96E−16 | 5.67E−11 | 2.43E−13 | 1.44E−11 | 1.99E+29 | 1.45E+32 | 294 | 0.404 | Hébrard et al. (2016) |

**Note.** Listed are the dipole, quadrupole, and octopole field strengths, mass-loss rates, spin-down torque, spin-down timescale, and paper in which the ZDI map of each star was originally published. For quantities with multiple estimates, the method used is noted in brackets.
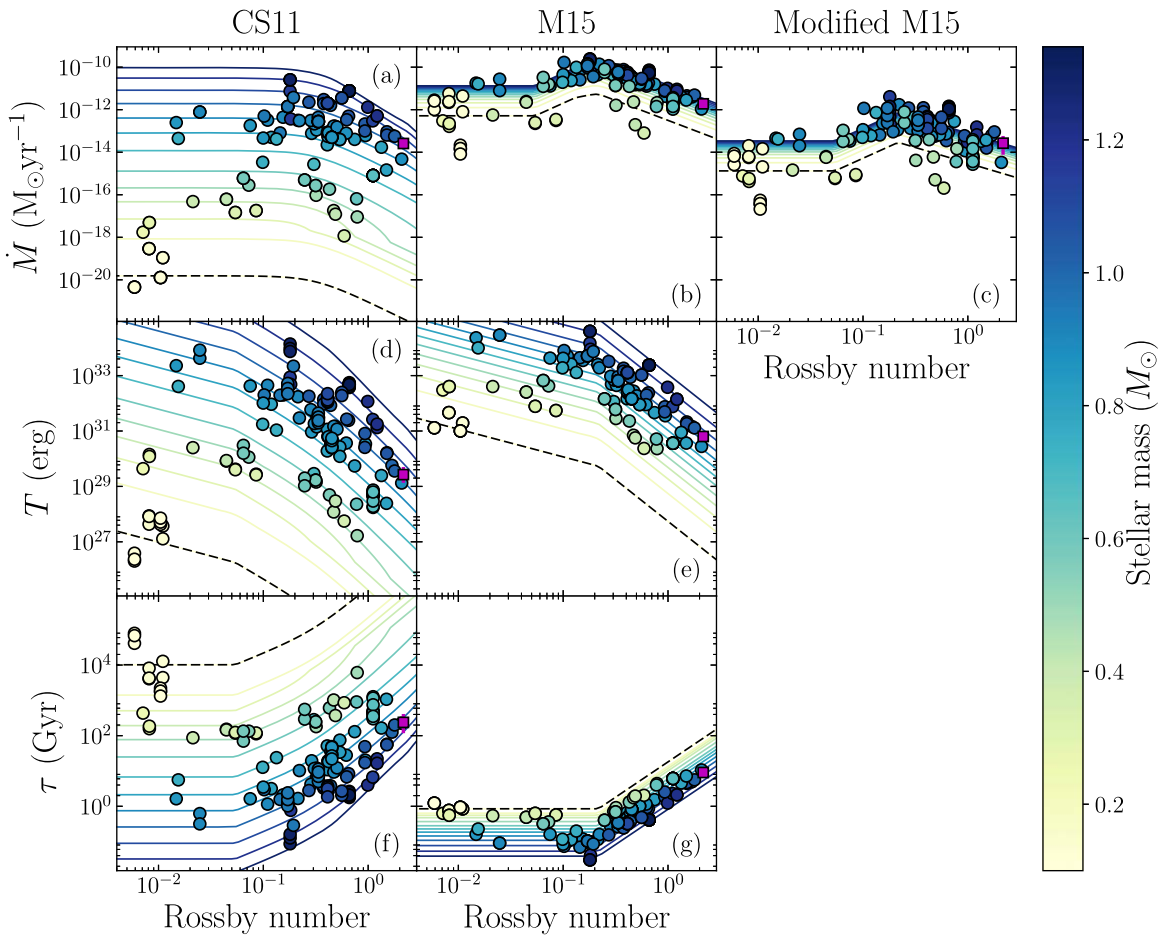
**Figure 3.** Mass-loss rate (top), angular momentum loss rate (middle), and spin-down timescale (bottom) as a function of Rossby number. These quantities are calculated using (or are associated with) the CS11 (left), M15 (middle), and modified M15 (right) models. Each point is color-coded by stellar mass. Solid lines correspond to the parameter of interest in each panel calculated for a given stellar mass over a range of Rossby numbers (see text for details). The solid lines are plotted in intervals of $0.1M_\odot$ from 0.1 to $1.3M_\odot$ and are also color-coded by stellar mass. The lines corresponding to $0.1M_\odot$ have been plotted with a dashed black line for visibility. The average solar value in each panel is shown with a magenta square, and the range of variability is shown with a magenta bar when applicable.

and luminosity are only a function of mass, not age or rotation, when calculating these curves, which is approximately true on the main sequence. This method produces radius and luminosity estimates that are broadly representative of the stars we are interested in. Although it is a relatively simple method of estimating radii and luminosities, it is appropriate, since the curves are simply illustrative and included only to help the reader interpret the data points. Overall, the data points in Figure 3 follow the trends shown by the lines, although there will be small deviations due to a number of different factors, e.g., the fact that the stars in our sample have a range of ages. For a given stellar mass, we see that the mass-loss rates follow the activity–rotation relation shape described in Section 3. The most striking feature is the range of predicted mass-loss rates, spanning around 10 orders of magnitude. The main determinant of the mass-loss rate for the CS11 model is the stellar mass, with rotation (or Rossby number) having a secondary effect.

Using these mass-loss rates, we can calculate torques, $T_{CS11}$, and spin-down timescales, $\tau_{CS11}$. Here $T_{CS11}$ is calculated using the F18 braking law (Equation (2)) and shown in Figure 3(d), while $\tau_{CS11}$ is given by $I_\star\Omega_\star/T_{CS11}$, where $I_\star$ is the moment of inertia of the star. Again, we use the stellar evolution models of Baraffe et al. (2015) to obtain moments of inertia for our

sample of stars. The $\tau_{CS11}$ is plotted in Figure 3(f). Similar to the mass-loss rate, we have plotted $T_{CS11}$ and $\tau_{CS11}$ curves in panels (d) and (f). When calculating the $T_{CS11}$ curves, we used the fits to our magnetic field data (Equation (4)) to determine the magnetic properties required in Equation (2). Due to the low mass-loss rates estimated by this model and the correspondingly low torques, the characteristic spin-down timescales are large, especially at the lowest masses. Given that M dwarfs are known to spin down on timescales shorter than those shown in Figure 3(f) (e.g., Douglas et al. 2017), one might interpret the large $\tau_{CS11}$ values for M dwarfs as evidence that the CS11 model substantially underestimates the mass-loss rates for low-mass stars.

### 4.2. Rotation Evolution Method

Our second method is to determine the mass-loss rate required by the F18 braking law in order to reproduce the rotation period evolution seen in open clusters. We will base this on the rotation period evolution model of Matt et al. (2015, hereafter M15), which was tuned to broadly reproduce observed rotation period distributions in open clusters; e.g., see their Figure 2. As discussed in Section 3, many forms of

magnetic activity can be parameterized in terms of the Rossby number but with different scalings depending on whether the star is in the so-called saturated or unsaturated regime. Motivated by this idea, Matt et al. (2015) assumed that magnetic terms in their spin-down torque can also be parameterized by Rossby number with different scalings in the saturated and unsaturated regimes (see their Equations (4) and (5)). The resulting torque has the form

$$T = 100 \, T_0 \left( \frac{\Omega_\star}{\Omega_\odot} \right) \qquad \text{for Ro} < \text{Ro}_{\text{crit}}$$

$$T = T_0 \left( \frac{\tau_{\text{cz}}}{\tau_{\text{cz}\odot}} \right)^2 \left( \frac{\Omega_\star}{\Omega_\odot} \right)^3 \qquad \text{for Ro} \geqslant \text{Ro}_{\text{crit}}. \qquad (5)$$

Here $T_0$ is an additional mass- (and radius-) dependent factor that is given by

$$T_0 = 6.3 \times 10^{30} \, \text{erg} \left( \frac{r_\star}{r_\odot} \right)^{3.1} \left( \frac{M_\star}{M_\odot} \right)^{0.5}. \qquad (6)$$

This additional mass dependence is required to explain observations that show that the lowest-mass stars take much longer to spin down compared to their higher-mass counterparts. For their critical Rossby number, M15 chose $\text{Ro}_{\text{crit}} = 0.2$. It is worth noting that this value is larger than the $\text{Ro}_{\text{crit}}$ values we obtained in our three-parameter fits in Section 3. For the Sun, this model estimates a spin-down torque of $6.3 \times 10^{30}$ erg, which is the value one finds if one assumes the Sun is a solid body and spinning down according to Skumanich (1972), i.e., $\Omega \propto t^{-1/2}$ (see Section 4.3 of F18, for further details). This value for the solar spin-down torque is similar to the values used in other rotation evolution models (see Figure 1 of Matt et al. 2015, for a comparison).

In Figure 3(e), we plot the torque for our sample using Equation (5). These torques are larger than those estimated using the CS11 model (Figure 3(d)), with the largest disagreement occurring for the lowest-mass stars. In Figure 3(b), we plot the mass-loss rate required by the F18 braking law to reproduce the torque used by M15, i.e., the mass-loss rate at which Equations (1) and (2) equal Equation (5). These mass-loss rates are much higher than those estimated using the CS11 model. This is unsurprising given the lower torques estimated when using the CS11 mass-loss rates. Lastly, we plot the spin-down timescale associated with this model, $\tau_{\text{M15}}$, in Figure 3(g). The $\tau_{\text{M15}}$ values are generally smaller than the $\tau_{\text{CS11}}$ values due to the larger $T_{\text{CS11}}$ values.

### 4.3. Modified Rotation Evolution Method

There is a striking problem with the model presented in Section 4.2. If one calculates the solar spin-down torque using the F18 braking law and the observed solar mass-loss rate, one obtains a value of $T = 2.5 \times 10^{29}$ erg, which is a factor of 25 smaller than the value predicted by the rotation evolution model of Matt et al. (2015). Conversely, if one calculates the mass-loss rate for the Sun in the manner described in Section 4.2, using the parameters from Table 1, one obtains a value of $\dot{M} = 1.8 \times 10^{-12} M_\odot \, \text{yr}^{-1}$. This is a factor of ~70 bigger than the observed solar mass-loss rate. Additionally, this method also estimates mass-loss rates that are much larger than
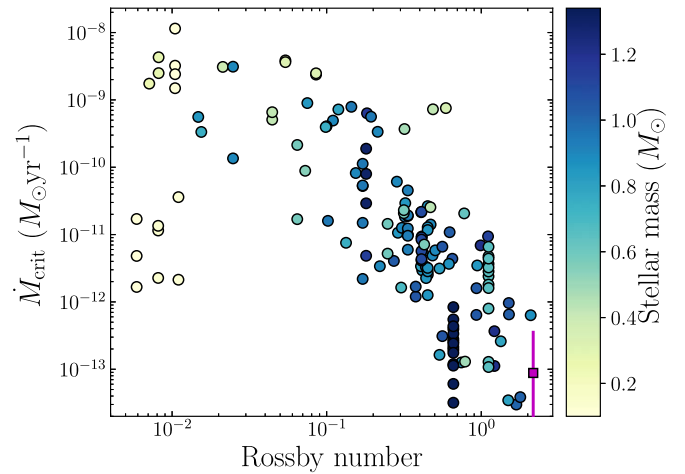


**Figure 4.** Critical mass-loss rate (Equation (3)) against Rossby number. Points are color-coded by stellar mass. The average solar $\dot{M}_{\text{crit}}$ is shown with a magenta square, and the range over cycle 24 is shown by the magenta bar. The lower limit of this range extends off the plot and has a value of $\dot{M}_{\text{crit}} = 5.7 \times 10^{-16} M_\odot \, \text{yr}^{-1}$ (the full range and variability of the magenta bar is shown by the magenta curve in Figure 6). For each star, the angular momentum loss rate is dominated by the dipole component of the stellar magnetic field if its actual mass-loss rate is below the critical mass-loss rate shown here.

the mass-loss rates inferred from Ly$\alpha$ observations (see Vidotto et al. 2016 for a sample of stars that have both ZDI maps and mass-loss rates inferred from Ly$\alpha$ observations). Clearly, there is a discrepancy between the F18 braking law and the rotation evolution models (also see discussion in Finley et al. 2018, 2019).

Although the origin of this discrepancy is unclear, one possible explanation is that the MHD models used by F18 may underpredict the torques. One solution is to include a multiplicative correction factor in the F18 braking law. In Figure 3(c), we recalculate mass-loss rates using the method from Section 4.2 but including a multiplicative factor of 25 in the F18 braking law. This value is chosen such that the solar mass-loss rate is recovered when using the method described in Section 4.2 for the Sun. Including the multiplicative factor reduces the estimated mass-loss rates by a factor of between 50 and 390, the value of which depends on the values of $\langle B_{\text{ZDI,d}} \rangle$, $\langle B_{\text{ZDI,q}} \rangle$, and $\langle B_{\text{ZDI,o}} \rangle$ for each star. We note that if the F18 braking law does underestimate spin-down torques by a factor of 25, then the torques in Figure 3(d) should all be larger by this amount.

## 5. Critical Mass-loss Rates

Having estimated mass-loss rates in Section 4, we can now compare them to the critical mass-loss rates as defined in Section 2. Figure 4 shows that the overall trend is for the critical mass-loss rate to decrease as a function of Rossby number. This decrease can be attributed to the dependence of $\dot{M}_{\text{crit}}$ on $B_\star^2$ (see Equation (3)). Physically, this is because stars with strong magnetic fields require a correspondingly large mass-loss rate for the Alfvén radius to be small enough for non-dipolar fields to contribute to the spin-down torque. There is also a large amount of scatter in Figure 4 that can be attributed to the scatter in $B_\star^2$, $\mathcal{R}_{\text{d}}$, and $\mathcal{R}_{\text{q}}$. Lastly, there is a departure from the overall trend at the lowest Rossby numbers that is
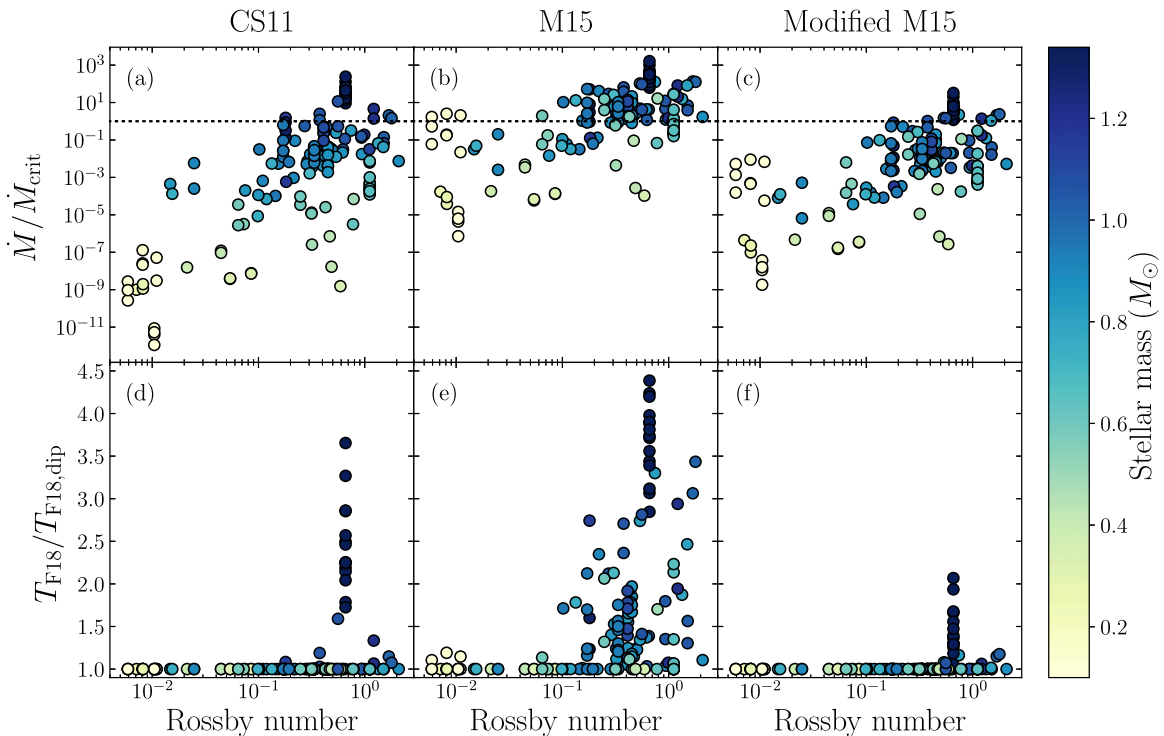
**Figure 5.** Top: ratio of mass-loss rate to critical mass-loss rate against Rossby number. Points above the dotted $\dot{M} = \dot{M}_{\rm crit}$ line have a non-dipolar field contribution to spin-down torque. Bottom: ratio of the torque calculated using the F18 braking law to the torque calculated using just the dipole component of the F18 braking law against Rossby number. Both quantities are calculated using the CS11 (left), rotation evolution (middle), and modified rotation evolution (right) methods. Points are color-coded by stellar mass.

caused by the bimodal magnetic fields of the lowest-mass M dwarfs (Donati et al. 2008; Morin et al. 2008b, 2010).

In the top row of Figure 5, we show the ratio of the mass-loss rate to the critical mass-loss rate against Rossby number for each of the mass-loss rate estimates outlined in Section 4. The dotted lines indicate $\dot{M} = \dot{M}_{\rm crit}$. For the CS11 model, we find that the majority of the stars have $\dot{M} < \dot{M}_{\rm crit}$, and, consequently, only the dipole component of the field is required to properly estimate the torque using the F18 braking law for most stars using this method. The few stars that do have $\dot{M} > \dot{M}_{\rm crit}$ are the highest-mass stars, since the mass-loss rates estimated by the CS11 model have a strong dependence on stellar mass. It should be noted that a significant number of the points in the $\dot{M} > \dot{M}_{\rm crit}$ regime are for one star, $\tau$ Boo. This is the star that we have the most ZDI maps for and is also the highest-mass star in our sample. In contrast to the CS11 model, a majority of the stars have $\dot{M} > \dot{M}_{\rm crit}$ when using the rotation evolution method (M15) to estimate mass-loss rates. However, as discussed in Section 4.3, these mass-loss rates are likely to be too high. Using the modified rotation evolution method to estimate mass-loss rates results in a significant reduction in the number of stars that have $\dot{M} > \dot{M}_{\rm crit}$.

Figure 5 demonstrates that there may be regimes where the mass-loss rates of low-mass stars are sufficiently high that non-dipolar field modes need to be accounted for to properly calculate their spin-down torques. It will be interesting to determine how different the spin-down torques for these stars are if we only account for their dipole fields. In the bottom row of Figure 5, we plot the ratio of the torque calculated using the full F18 braking law, $T_{\rm F18}$, to the torque calculated using just the dipole component, $T_{\rm F18,dip}$, i.e., Equation 2(a). This ratio is

calculated using the mass-loss rate estimates from Section 4, i.e., the mass-loss rates shown in Figures 3(a)–(c). By definition, this ratio is equal to 1 when $\dot{M} < \dot{M}_{\rm crit}$. However, when $\dot{M} > \dot{M}_{\rm crit}$, $T_{\rm F18}$ is bigger than $T_{\rm F18,dip}$. This can be seen in Figure 1, where the dipole-only line (red dotted–dashed line) drops below the upper envelope of the three curves for $\dot{M} > \dot{M}_{\rm crit}$. Physically, the reason that $T_{\rm F18} > T_{\rm F18,dip}$ is because the Alfvén radii are sufficiently small at high mass-loss rates for the non-dipolar fields to contribute to the spin-down torque. However, since $T_{\rm F18,dip}$ does not account for the flux in non-dipolar modes, the resulting torque is smaller. The $T_{\rm F18}/T_{\rm F18,dip}$ can reach values of around 3.7, 4.4, and 2.1, respectively, for the CS11, M15 and modified M15 methods. However, this is skewed by $\tau$ Boo. If we put $\tau$ Boo aside, $T_{\rm F18}/T_{\rm F18,dip}$ never exceeds 1.6 for the CS11 and modified M15 methods.

It is interesting to note that, generally, the non-dipolar field modes only become important at large Rossby numbers. For the CS11 method, this is mainly an effect of the stellar mass. As already noted, the stars with the highest mass-loss rates, i.e., those most likely to have $\dot{M} > \dot{M}_{\rm crit}$, are the highest-mass stars. In our sample, these happen to be the ones with the largest Rossby numbers. For the rotation evolution and modified rotation evolution models, the explanation is slightly different. We have already noted that the critical mass-loss rate has a dependence on $B_\star^2$. For these models, both $\dot{M}$ (for a given mass) and $B_\star^2$ decrease as a function of Rossby number in the unsaturated regime. However, $B_\star^2$, and hence $\dot{M}_{\rm crit}$, decreases more steeply than $\dot{M}$. As such, broadly speaking, $\dot{M}$ becomes larger than $\dot{M}_{\rm crit}$ as the Rossby number increases. This also predicts that Alfvén radii decrease as stars spin down.

## 6. Uncertainties

In this section, we discuss the uncertainties, caveats, and open questions relating to the methods and models we have used in this paper, as well as where future progress may impact our conclusions.

### 6.1. ZDI

Modern ZDI codes express magnetic fields in terms of a spherical harmonic decomposition (e.g., see Appendix B of Folsom et al. 2018a). It is well known that ZDI does not recover the magnetic field associated with small-scale structures, e.g., star spots, due to flux cancellation effects (Reiners & Basri 2009; Morin et al. 2010; See et al. 2019). Typically, ZDI maps have a maximum spherical harmonic degree of $\ell_{max} = 5$–15. Lehmann et al. (2019) recently showed that even the field strengths associated with low-order $\ell$ modes, including the dipole, quadrupole, and octopole modes, can be systematically underestimated by factors of a few by ZDI. The possibility of underestimated field strengths has two main consequences for our results.

The first consequence is that the spin-down torque will be underestimated due to the dependence of the F18 braking law on magnetic field strength. Underestimated field strengths may partially alleviate a problem noted by Finley et al. (2019). Similar to this work, these authors estimated the spin-down torques for a number of stars with ZDI maps using the F18 braking law. However, they used mass-loss rates inferred from Ly$\alpha$ observations (see, e.g., Wood et al. 2014). The torques they estimated using the F18 braking law were smaller than the torques estimated by the M15 rotation evolution model by a factor of ∼3–30. Closer agreement between these two torque estimates could be achieved if the dipolar, quadrupolar, and octopolar field strengths are larger than those inferred by ZDI. Their results are also consistent with our results from Section 4.2. The mass-loss rates we estimate using the rotation evolution method are much larger than those inferred from Ly$\alpha$. As with the results of Finley et al. (2019), the discrepancy between rotation evolution–based estimates of stellar torques and braking law–based estimates can be partially alleviated by larger field strengths. However, it is unlikely that the discrepancy can be fully accounted for by underestimated field strengths from ZDI.

The second consequence relates to the fact that $\dot{M}_{crit} \propto B_\star^2$. If the true field strengths are a factor of several higher than that recovered by ZDI, the critical mass-loss rate would increase by roughly an order of magnitude. Consequently, even fewer stars than suggested in Section 5 will have $\dot{M} > \dot{M}_{crit}$.

### 6.2. Mass-loss Rate Estimates

Estimating mass-loss rates is notoriously difficult because the mechanisms that drive stellar winds are still poorly understood. Although the CS11 model is one of the more sophisticated models currently available for estimating mass-loss rates, it still has limitations. It is based on many previous observations and theoretical works, and uncertainty in those works will propagate through into the final mass-loss rate estimate. For example, one key part of the model that remains relatively unconstrained is the magnetic characteristics of low-mass stars. Parameters such as the amount of energy flux in Alfvén waves, the fraction of the stellar surface covered in open flux tubes, and the rate at which these flux tubes expand above the stellar surface all play an important role in determining the overall mass-loss rate but remain uncertain. Other details, such as the terminal wind speed or the location of the transition region, are also hard to determine reliably and will contribute to the overall uncertainty of this model. We refer the interested reader to Section 6 of CS11 for a much more comprehensive discussion of these uncertainties.

Our second method of estimating mass-loss rates relies on rotation period evolution models. Although models are now able to capture the overall rotation evolution behavior of low-mass stars, none can yet fit all of the available data. Additionally, the rotation evolution models are not well constrained in areas of parameter space where rotation period data are sparse, particularly for the lowest-mass and oldest stars. In the model of Matt et al. (2015), the rotation periods of the lowest-mass stars are not reproduced well, which can be seen when comparing the model to observations from the Hyades (see Figure 14 in Douglas et al. 2016) and Praesepe (see Figure 11 in Douglas et al. 2017). Outside of the lowest-mass M dwarfs, the disagreement between the M15 model and observed rotation periods can be up to ∼50% in some mass and age ranges. Our mass-loss rate estimates that are based on the rotation evolution models (Section 4.3) will therefore be correspondingly uncertain. However, since the model reproduces the broad features seen in rotation period distributions with a relatively simple torque prescription, it is ideal for the purposes of this work.

### 6.3. Stellar Variability

In this work, we have estimated mass-loss and angular momentum loss rates at single instances in time (or at a few instances for stars with multiple ZDI maps). However, stellar magnetic activity is known to be time-variable. Therefore, their mass-loss and angular momentum loss rates are also time-variable. For example, the angular momentum loss rate of the Sun is expected to vary over a range of timescales (Pinto et al. 2011; Réville & Brun 2017; Finley et al. 2018; Perri et al. 2018). As noted in Section 2, the Sun has a mass-loss rate that is smaller than its critical mass-loss rate. However, that was calculated using averages of the solar dipolar, quadrupolar, and octopolar fields over ∼8 yr using the data from Vidotto et al. (2018). In the top panel of Figure 6, we show the critical mass-loss rate as a function of time for the Sun. This is done using data from Vidotto et al. (2018) and Finley et al. (2018) shown in magenta and blue, respectively.[15] From 2010 to 2018, where data are available from both studies, the two critical mass-loss rate estimates are broadly comparable. We also plot the solar mass-loss rate determined from in situ spacecraft measurements (Finley et al. 2018) with a black line. Times when the mass-loss rate exceeds the critical mass-loss rate (estimated from the Finley et al. 2018 data) are shaded in gray. For reference, the bottom panel shows the sunspot number indicating periods of maximum activity around 2001 and 2013. We see that the solar mass-loss rate does not exceed the critical mass-loss rate for the majority of the last two solar cycles, suggesting that the dipole

---

[15] The solar magnetograms of Vidotto et al. (2018) consist of the radial, meridional, and azimuthal components, while Finley et al. (2018) only consider the radial component in their work. So far in this work, we have used the magnetograms of Vidotto et al. (2018) because they provide a better comparison to ZDI maps that also contain all three vector components. However, the data set studied by Finley et al. (2018) covers a longer time period, so we have included both in Figure 6.
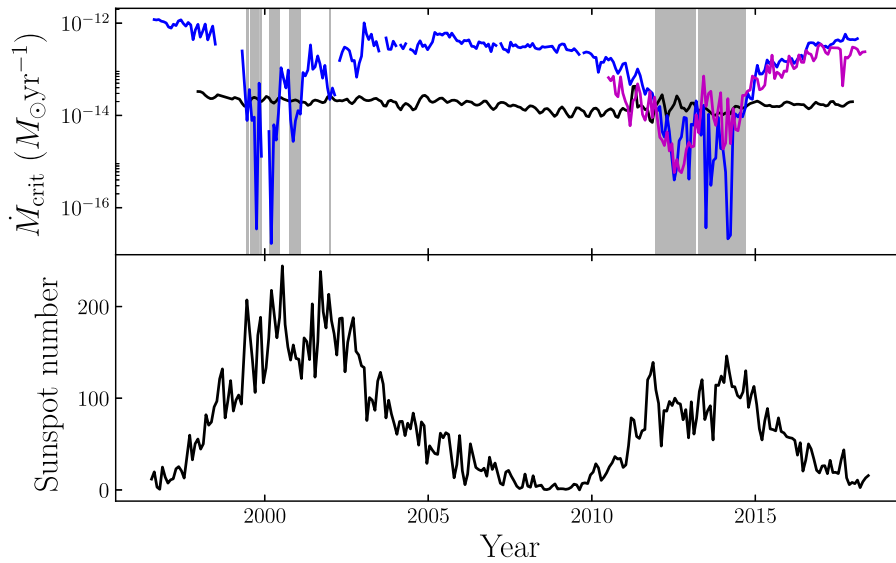
**Figure 6.** Top: critical mass-loss rate for the Sun calculated using magnetic data from Vidotto et al. (2018; magenta line) and Finley et al. (2018; blue line). The solar mass-loss rate estimated by F18 is also shown (black line). Regions where the mass-loss rate is greater than the critical mass-loss rate are shaded in gray. Bottom: sunspot number.

**Table 3**
Best-fit Parameters for Equation (4)

|  | $B_{\mathrm{sat,i}}$ | $\mathrm{Ro}_{\mathrm{crit,i}}$ | $\beta_i$ |
| --- | --- | --- | --- |
| Dipole | $137 \pm 48$ | $0.05 \pm 0.02$ | $-1.31 \pm 0.10$ |
| Quadrupole | $73 \pm 21$ | $0.05 \pm 0.01$ | $-1.25 \pm 0.08$ |
| Octopole | $65 \pm 17$ | $0.05 \pm 0.01$ | $-1.37 \pm 0.09$ |

magnetic field dominates the solar torque most of the time. However, the non-dipolar components become important around solar maximum. This is due to the growing quadrupolar field and shrinking dipolar field at solar maximum (DeRosa et al. 2012).

The magnetic fields of stars that have been mapped with ZDI over multiple epochs are also known to evolve over time (e.g., Jeffers et al. 2014; Boro Saikia et al. 2016, 2018; Lavail et al. 2018). Correspondingly, their estimated torques also change as a function of time. As with the Sun, this means other stars can spend some times with $\dot{M} > \dot{M}_{\mathrm{crit}}$ and other times with $\dot{M} < \dot{M}_{\mathrm{crit}}$. In the context of long-term rotation period evolution, models are only sensitive to the spin-down torque averaged over timescales of Myr or more, so comparisons with instantaneous torque estimates will always be uncertain.

### 6.4. Braking Law

While the F18 braking law allows for a rapid assessment of the spin-down torque of a star, there are still areas in which it can be improved. For instance, the MHD simulations on which this braking law is based assume a fixed coronal temperature and use the polytropic assumption, which can have a small impact on the resulting wind solutions (Pantolmos & Matt 2017). Additionally, F18 only investigated axisymmetric field configurations, while we have also included nonaxisymmetric field components in this work. By using the F18 braking law, we have effectively moved power from the nonaxisymmetric modes to the axisymmetric ones. Although the effect of including nonaxisymmetric modes into braking law studies like that of F18 is not entirely understood, we do not expect that it

will drastically change our results (also see Section 5.1 of Finley et al. 2018).

Lastly, using *Ulysses* data, Finley et al. (2018) showed that the simulations used to construct the F18 braking law appear to underestimate the open flux for a given input solar magnetogram. This problem is not unique to the F18 simulations (e.g., Linker et al. 2017). Correspondingly, the F18 spin-down torque estimates are also probably underestimated by a factor of a few just due to the open flux problem. The reason for this is not clear, but any potential solution may increase the contribution of non-dipolar modes to the spin-down torque. In order to increase the open flux, the height of the last closed field loop must decrease (this radius is variously called the opening radius or source surface radius in the literature, depending on the context). Since non-dipolar fields decay more rapidly than dipolar fields as a function of radius, the contribution of non-dipolar modes to the open flux is increased by opening up magnetic flux closer to the stellar surface. Unfortunately, it is currently difficult to quantify the magnitude of this effect, but it should be kept in mind.

### 7. Discussion and Conclusion

Using a sample of stars that have been mapped with ZDI and the braking law of F18, we have investigated whether non-dipolar magnetic fields contribute significantly to stellar spin-down. In order to use this braking law, mass-loss rates have to be estimated for each of the stars. In general, large mass-loss rates are required for non-dipolar fields to contribute to stellar spin-down. We quantify this in terms of a critical mass-loss rate, $\dot{M}_{\mathrm{crit}}$, that depends on the field strength and geometry of the star. If a star has a mass-loss rate smaller than $\dot{M}_{\mathrm{crit}}$, only the dipolar field mode is required to calculate the spin-down torque. However, higher-order field modes need to be accounted for when stars have mass-loss rates larger than $\dot{M}_{\mathrm{crit}}$. We used two methods to estimate the mass-loss rate.

The first method uses the model of Cranmer & Saar (2011). Using these mass-loss rates, we find that the non-dipolar magnetic field modes do not contribute to spin-down for the majority of the stars in our sample. The stars that do have mass-

loss rates larger than $\dot{M}_{crit}$ are the highest-mass stars in our sample. This is due to the strong dependence of mass-loss rate on stellar mass in the Cranmer & Saar (2011) model.

The second method estimates mass-loss rates by determining the mass-loss rates required by the F18 braking law to reproduce the spin-down torques from the rotation evolution model of Matt et al. (2015). This method produces much higher mass-loss rates than the model of Cranmer & Saar (2011). Consequently, a majority of the sample has mass-loss rates larger than $\dot{M}_{crit}$. However, this method overestimates the solar mass-loss rate. This is likely because the Finley & Matt (2018) braking law is underpredicting the spin-down torque. To reproduce the observed solar mass-loss rate using this method, a multiplicative factor of 25 needs to be included in the Finley & Matt (2018) braking law. Once this is included, far fewer stars have mass-loss rates that exceed $\dot{M}_{crit}$. In this model, the stars where high-order field modes need to be accounted for are those at large Rossby numbers.

Our core conclusion is therefore that non-dipolar magnetic fields do not contribute significantly to stellar spin-down for the majority of low-mass stars. However, there are stars in some parameter regimes, whose mass-loss rates are estimated to be particularly large, for which this may not be true. This result is based on the mass-loss rate estimates of two models, although one could, in principle, conduct this sort of study using any mass-loss rate model. Indeed, different methods of estimating mass-loss rates may predict different parameter regimes in which non-dipolar fields need to be accounted for. It is also worth noting that this conclusion assumes that the mass-loss rate of a star is known. In reality, small-scale fields are important for heating and determining the mass-loss rate (e.g., Cranmer & Saar 2011; Suzuki et al. 2013). However, for a given mass-loss rate, only the dipole field is important for stellar spin-down for most stars.

Lastly, it is worth discussing our results in the context of rotation evolution models. In recent years, higher magnetic field complexity has been invoked when a reduced torque is required by rotation evolution models to fit the observed period distributions in open clusters. The justification for this is that MHD simulations have shown that, all else being equal, stars with higher-order spherical harmonic field modes have vastly reduced torques (Réville et al. 2015; Garraffo et al. 2016). For example, Garraffo et al. (2018) cited the higher field complexity of rapid rotators as evidence that they should also have reduced spin-down torques. However, the MHD simulations for computing torques conducted before those of Finley & Matt (2017, 2018) have generally only considered a single spherical harmonic order in each simulation. In reality, the magnetic fields of stars are a superposition of many spherical harmonic modes. While it is true that some stars within our sample have more magnetic energy at higher-order spherical harmonic modes, i.e., fields associated with smaller spatial scales, all of the stars contain a nonnegligible dipole component (see Figure 2(a)). This is the reason why non-dipolar modes do not significantly contribute to stellar spin-down for the majority of our stars.

## ORCID iDs

Victor See https://orcid.org/0000-0001-5986-3423
Sean P. Matt https://orcid.org/0000-0001-9590-2274
Adam J. Finley https://orcid.org/0000-0002-3020-9409
Moira M. Jardine https://orcid.org/0000-0002-1466-5236
Julien Morin https://orcid.org/0000-0002-4996-6901
Aline A. Vidotto https://orcid.org/0000-0001-5371-2675

## References

Amard, L., Palacios, A., Charbonnel, C., Gallet, F., & Bouvier, J. 2016, A&A, 587, A105
Baraffe, I., Homeier, D., Allard, F., & Chabrier, G. 2015, A&A, 577, A42
Blackman, E. G., & Owen, J. E. 2016, MNRAS, 458, 1548
Boro Saikia, S., Jeffers, S. V., Morin, J., et al. 2016, A&A, 594, A29
Boro Saikia, S., Jeffers, S. V., Petit, P., et al. 2015, A&A, 573, A17
Boro Saikia, S., Lueftinger, T., Jeffers, S. V., et al. 2018, A&A, 620, L11
Brown, S. F., Donati, J.-F., Rees, D. E., & Semel, M. 1991, A&A, 250, 463
Brown, T. M. 2014, ApJ, 789, 101
Cranmer, S. R., & Saar, S. H. 2011, ApJ, 741, 54
DeRosa, M. L., Brun, A. S., & Hoeksema, J. T. 2012, ApJ, 757, 96
do Nascimento, J.-D., Jr., Vidotto, A. A., Petit, P., et al. 2016, ApJL, 820, L15
Donati, J.-F., & Brown, S. F. 1997, A&A, 326, 1135
Donati, J.-F., Collier Cameron, A., Semel, M., et al. 2003, MNRAS, 345, 1145
Donati, J.-F., Howarth, I. D., Jardine, M. M., et al. 2006, MNRAS, 370, 629
Donati, J.-F., Morin, J., Petit, P., et al. 2008, MNRAS, 390, 545
Douglas, S. T., Agüeros, M. A., Covey, K. R., et al. 2016, ApJ, 822, 47
Douglas, S. T., Agüeros, M. A., Covey, K. R., & Kraus, A. 2017, ApJ, 842, 83
Fares, R., Donati, J.-F., Moutou, C., et al. 2009, MNRAS, 398, 1383
Fares, R., Donati, J.-F., Moutou, C., et al. 2010, MNRAS, 406, 409
Fares, R., Donati, J.-F., Moutou, C., et al. 2012, MNRAS, 423, 1006
Fares, R., Moutou, C., Donati, J.-F., et al. 2013, MNRAS, 435, 1451
Finley, A. J., & Matt, S. P. 2017, ApJ, 845, 46
Finley, A. J., & Matt, S. P. 2018, ApJ, 854, 78
Finley, A. J., Matt, S. P., & See, V. 2018, ApJ, 864, 125
Finley, A. J., See, V., & Matt, S. P. 2019, ApJ, 876, 44
Folsom, C. P., Bouvier, J., Petit, P., et al. 2018a, MNRAS, 474, 4956
Folsom, C. P., Fossati, L., Wood, B. E., et al. 2018b, MNRAS, 481, 5286
Folsom, C. P., Petit, P., Bouvier, J., et al. 2016, MNRAS, 457, 580
Gallet, F., & Bouvier, J. 2013, A&A, 556, A36
Gallet, F., & Bouvier, J. 2015, A&A, 577, A98
Garraffo, C., Drake, J. J., & Cohen, O. 2015, ApJL, 807, L6
Garraffo, C., Drake, J. J., & Cohen, O. 2016, A&A, 595, A110
Garraffo, C., Drake, J. J., Dotter, A., et al. 2018, ApJ, 862, 90
Gondoin, P. 2017, A&A, 599, A122
Hébrard, É. M., Donati, J.-F., Delfosse, X., et al. 2016, MNRAS, 461, 1465
Jardine, M., & Collier Cameron, A. 2019, MNRAS, 482, 2853
Jardine, M., Vidotto, A. A., & See, V. 2017, MNRAS, 465, L25
Jeffers, S. V., Petit, P., Marsden, S. C., et al. 2014, A&A, 569, A79
Johnstone, C. P., Güdel, M., Brott, I., & Lüftinger, T. 2015, A&A, 577, A28
Lavail, A., Kochukhov, O., & Wade, G. A. 2018, MNRAS, 479, 4836
Lehmann, L. T., Hussain, G. A. J., Jardine, M. M., Mackay, D. H., & Vidotto, A. A. 2019, MNRAS, 483, 5246
Linker, J. A., Caplan, R. M., Downs, C., et al. 2017, ApJ, 848, 70
Marsden, S. C., Jardine, M. M., Ramírez Vélez, J. C., et al. 2011, MNRAS, 413, 1922
Matt, S. P., Brun, A. S., Baraffe, I., Bouvier, J., & Chabrier, G. 2015, ApJL, 799, L23

Mengel, M. W., Fares, R., Marsden, S. C., et al. 2016, MNRAS, 459, 4325
Morgenthaler, A., Petit, P., Saar, S., et al. 2012, A&A, 540, A138
Morin, J., Donati, J.-F., Forveille, T., et al. 2008a, MNRAS, 384, 77
Morin, J., Donati, J.-F., Petit, P., et al. 2008b, MNRAS, 390, 567
Morin, J., Donati, J.-F., Petit, P., et al. 2010, MNRAS, 407, 2269
Pantolmos, G., & Matt, S. P. 2017, ApJ, 849, 83
Perri, B., Brun, A. S., Réville, V., & Strugarek, A. 2018, JPlPh, 84, 765840501
Petit, P., Dintrans, B., Solanki, S. K., et al. 2008, MNRAS, 388, 80
Pinto, R. F., Brun, A. S., Jouve, L., & Grappin, R. 2011, ApJ, 737, 72
Pizzolato, N., Maggio, A., Micela, G., Sciortino, S., & Ventura, P. 2003, A&A, 397, 147
Reiners, A., & Basri, G. 2009, A&A, 496, 787
Réville, V., & Brun, A. S. 2017, ApJ, 850, 45
Réville, V., Brun, A. S., Matt, S. P., Strugarek, A., & Pinto, R. F. 2015, ApJ, 798, 116
Sadeghi Ardestani, L., Guillot, T., & Morel, P. 2017, MNRAS, 472, 2590
See, V., Jardine, M., Vidotto, A. A., et al. 2017, MNRAS, 466, 1542
See, V., Jardine, M., Vidotto, A. A., et al. 2018, MNRAS, 474, 536
See, V., Matt, S. P., Folsom, C. P., et al. 2019, ApJ, 876, 118

Semel, M. 1989, A&A, 225, 456
Skumanich, A. 1972, ApJ, 171, 565
Stelzer, B., Damasso, M., Scholz, A., & Matt, S. P. 2016, MNRAS, 463, 1844
Suzuki, T. K., Imada, S., Kataoka, R., et al. 2013, PASJ, 65, 98
van Saders, J. L., Ceillier, T., Metcalfe, T. S., et al. 2016, Natur, 529, 181
Vidotto, A. A., & Bourrier, V. 2017, MNRAS, 470, 4026
Vidotto, A. A., Donati, J.-F., Jardine, M., et al. 2016, MNRAS, 455, L52
Vidotto, A. A., Jardine, M., Morin, J., et al. 2014, MNRAS, 438, 1162
Vidotto, A. A., Lehmann, L. T., Jardine, M., & Pevtsov, A. A. 2018, MNRAS, 480, 477
Waite, I. A., Marsden, S. C., Carter, B. D., et al. 2015, MNRAS, 449, 8
Waite, I. A., Marsden, S. C., Carter, B. D., et al. 2017, MNRAS, 465, 2076
Weber, E. J., & Davis, L., Jr. 1967, ApJ, 148, 217
Wood, B. E., Müller, H.-R., Redfield, S., & Edelman, E. 2014, ApJ, 781, L33
Wright, N. J., & Drake, J. J. 2016, Natur, 535, 526
Wright, N. J., Drake, J. J., Mamajek, E. E., & Henry, G. W. 2011, ApJ, 743, 48
Wright, N. J., Newton, E. R., Williams, P. K. G., Drake, J. J., & Yadav, R. K. 2018, MNRAS, 479, 2351